Nano Research

ISSN 1998-0124 CN 11-5974/O4
https://doi.org/10.26599/NR.2026.94909248

Research Article

A self-gelling and easily removable halloysite nanotubes/konjac glucomannan composite sponges for irregular hemorrhage control and wound healing

Xiaohui Yang[1,§](✉), Haibo Zheng[1,§], Shaokun Li[1], Yuxin Song[1], Mei Long[1](✉), Jun-Long Zhang[2](✉)

[1] School of Materials Science and Engineering, Guizhou Minzu University, Guiyang 550025, China

[2] Beijing National Laboratory for Molecular Sciences, College of Chemistry and Molecular Engineering, Peking University, Beijing 100871, China

[§] Xiaohui Yang and Haibo Zheng contributed equally to this work.

Nano Res., **Just Accepted Manuscript** • https://doi.org/10.26599/NR.2026.94909248

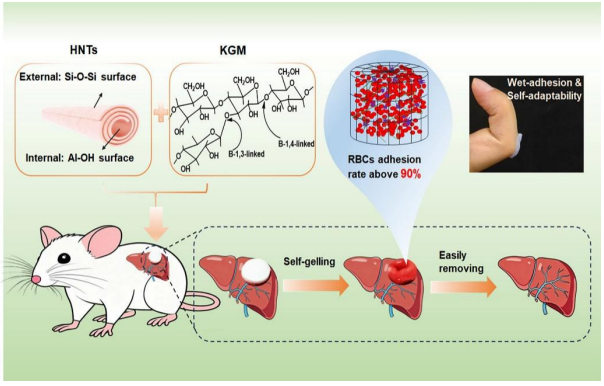
https://www.sciopen.com/journal/1998-0124 on Oct. 12, 2026

© The Authors(s)

Just Accepted

This is a "Just Accepted" manuscript, which has been examined by the peer-review process and has been accepted for publication. A "Just Accepted" manuscript is published online shortly after its acceptance,which is prior to technical editing and formatting and author proofing. Tsinghua University Press (TUP) provides "Just Accepted" as an optional and free service which allows authors to make their results available to the research community as soon as possible after acceptance. After a manuscript has been technically edited and formatted, and the page proofs have been corrected, it will be removed from the "Just Accepted" web site and published officially with volume and article number (e.g., *Nano Research*, **2025**, *18*, 94906990). Please note that technical editing may introduce minor changes to the manuscript text and/or graphics which may affect the content, and all legal disclaimers that apply to the journal pertain. In no event shall TUP be held responsible for errors or consequences arising from the use of any information contained in these "Just Accepted" manuscripts. To cite this anuscript please use its Digital Object Identifier (DOI®),which is identical for all formats of publication.

Just Accepted



A superior hemostatic platform based on nano-clay achieves rapid clotting, a 75.24% reduction in blood loss, and in situ self-gelation, enabling safe, one-piece removal without tissue adhesion.

Just Accepted

Nano Research

Open Access

Research Article

A self-gelling and easily removable halloysite nanotubes/konjac glucomannan composite sponges for irregular hemorrhage control and wound healing

Xiaohui Yang [1,§], Haibo Zheng [1,§], Shaokun Li [1], Yuxin Song [1], Mei Long [1], and Jun-Long Zhang [2]

[1] *School of Materials Science and Engineering, Guizhou Minzu University, Guiyang 550025, China*
[2] *Beijing National Laboratory for Molecular Sciences, College of Chemistry and Molecular Engineering, Peking University, Beijing 100871, China*
[§] *Xiaohui Yang and Haibo Zheng contributed equally to this work.*

Received: 4 June 2026; **Revised:** 19 September 2026; **Accepted:** 12 October 2026

Address correspondence to Xiaohui Yang, xiaohuiyang90@163.com; Mei Long, meilongcsu@163.com; Jun-Long Zhang, zhangjunlong@pku.edu.cn

Cite this article: *Nano Research*, 2026, 19, 94909248 https://doi.org/10.26599/NR.2026.94909248

ABSTRACT: Effective management of bleeding from irregular wounds requires materials with adaptability, wet adhesion and robust hemostatic capacity. We have developed a novel, self-gelling Halloysite Nanotubes/Konjac Glucomannan (HNTs/KGM) composite sponge that exhibits an in-situ sponge-to-hydrogel transition upon application. This design incorporates a dual-action mechanism: the KGM matrix serves as a scaffold for rapid blood cell concentration, while the HNTs function as potent activators of the coagulation cascade. In the preclinical models of severe liver hemorrhage and tail amputation, the optimized HNTs/KGM sponge achieved hemostasis, with blood loss reduced by 75.24% and 97.77%, respectively, demonstrating significantly superior performance compared to control groups. A notable clinical advantage lies in the sponge's one-piece removability post-hemostasis, which mitigates secondary damage associated with residual hemostatic powders, has the potential to facilitate wound healing. Additionally, the composite exhibited excellent cytocompatibility and hemocompatibility, with cell viability exceeding 95% and minimal hemolysis observed. Given its combination of rapid efficacy, superior operability, and robust safety profile, the HNTs/KGM sponge represents a promising candidate for next- generation hemostatic agents.

KEYWORDS: konjac glucomannan, halloysite nanotubes, hemostatic sponge, self-gelling, easily removable, irregular hemorrhage

Just Accepted

1 Introduction

Uncontrolled bleeding induced by severe trauma resulting from accidents, conflicts and natural disasters claims more than 2 million lives worldwide each year, and efficient hemostasis is the key to saving the lives of injured patients [1-3]. However, most wounds present irregular shapes, which renders conventional hemostatic materials difficult to adapt to wound configurations and incapable of achieving desirable hemostasis [3-5]. Consequently, there is therefore an urgent, unmet need for hemostatic materials capable of conforming to irregular shapes while actively accelerating the coagulation cascade.

Halloysite nanotubes (HNTs) represent a promising procoagulant candidate, capable of robustly activating the intrinsic coagulation cascade due to their unique hollow morphology and negatively charged surface [6-8]. However, a critical limitation has impeded their clinical translation, as free powders, HNTs are difficult to localize at the wound site and hard to eliminate after application, which poses risks of inflammation and embolism, thereby inducing secondary damage [9, 10]. While incorporation of HNTs into scaffold-based carrier systems (such as PET [11], PVA nanofibrous membranes [12], cotton fibers [13], and oxidized cellulose nanofibers [10]) can address the loss of powdered materials. Nevertheless, these composite systems generally lack the conformability and tissue adhesion necessary for effective sealing of a irregular wound.

Natural polysaccharides (such as chitosan [14, 15], sodium alginate [16, 17] and hyaluronan [18]) possess inherent biocompatibility and biodegradability, making them ideal carriers for hemostatic materials [19]. Numerous existing studies have demonstrated that the fabrication of hydrogels via compositing HNTs with natural polysaccharides [20-23], combined with strategies including 3D printing [14] and injectable administration [16], can effectively improve the conformability and tissue adhesion toward irregular wounds [19, 24, 25]. Nevertheless, their practical applications are still largely restricted by hydrogel formation conditions, as well as the requirements for printing inks or injectable formulations.

As a natural polysaccharide, konjac glucomannan (KGM) inherits the common advantages of general natural polysaccharides and possesses distinctive inherent properties, endowing it great potential as a hemostatic matrix [26, 27]. KGM's efficacy is rooted in three key attributes that are particularly well-suited for hemorrhage control. First, its structure is rich in hydrophilic hydroxyl groups, enabling rapid absorption of absorb plasma from blood, thereby concentrating platelets and clotting factors to

physically accelerate coagulation [28]. Second, this high affinity for water contributes to its excellent bio-adhesion, allowing it to anchor to moist tissue surfaces [29]. Finally, unlike most other polysaccharides, KGM exhibits outstanding gel-forming capacity [30, 31]. Upon water absorption, KGM can spontaneously form a gel. The resulting gel not only seals wounds effectively but also maintains a moist environment conducive to subsequent healing processes [32, 33]. These combined properties make KGM an ideal, biocompatible platform for developing a next-generation hemostatic agent [28, 34].

In this study, we report the design and fabrication of a novel, dual-action hemostatic agent in the form of as a self-gelling composite sponge created by integrating HNTs into a porous KGM matrix via freeze-drying (Scheme 1). We hypothesized that this design would synergistically combine the rapid blood absorption and conformable gelling properties of KGM with the potent biochemical activation of HNTs. This research presents a comprehensive evaluation of the sponge's physicochemical properties, biocompatibility, hemostatic performance and wound healing capacity through rigorous in vitro and in vivo testing. The results demonstrate that the sponge-to-hydrogel system is engineered for easy easily application, rapid conformability to the wound cavity, and the limitations of powdered hemostats by ensuring one-piece removability, and ultimately providing superior control of irregular bleeding.

2 Materials and methods

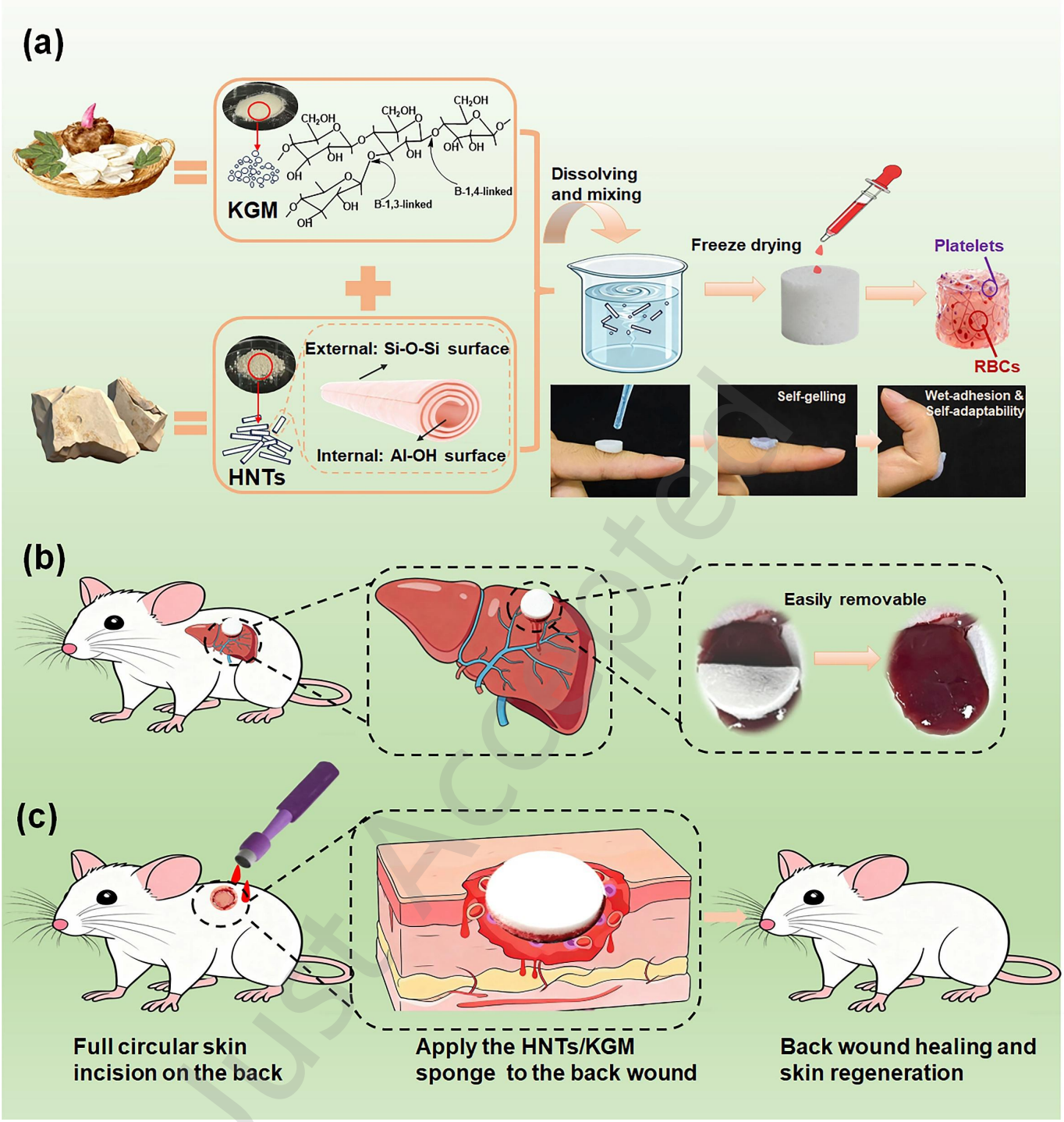
2.1 Materials

KGM (KJ36, purity 90%, viscosity 36000 mPa · s) was supplied by Hubei Konson Konjac Technology Co. Ltd. (Hubei, China). HNTs (molecular weight: 294.19g/mol, diam. × L: 30-70 nm × 1-3μm, purity ≧ 95%) were purchased from Sigma-Aldrich Co. Ltd. (America). Calcium chloride ($CaCl_2$) was supplied by Aladdin Reagent Co. Ltd. (Shanghai, China). Sodium citrate-anticoagulated whole blood, sourced from healthy New Zealand white rabbits and prepared at a 9:1 blood-to-anticoagulant ratio, was obtained from Guangzhou Hongquan Biotechnology Co. Ltd. (Guangdong, China).

2.2 Preparation of HNTs/KGM sponge

HNTs were added in 90°C distilled water and stirred for 10 min. Subsequently, KGM was gradually added and stirred into the HNTs suspension for 10 min. The mixture was then placed in a water bath at 90°C and allowed to swell for 30 min. Subsequently, the mixture was agitated at 90°C for 10 min and then dispensed into 24-well plates. Following this, the samples underwent a 12 h freezing period, after which they were subjected to lyophilization for 72 h. The HNTs/KGM composite sponges were prepared at HNTs-to-KGM mass ratios of 0:10, 1:10, 2:10, 4:10 and 6:10, denoted as pure KGM, H:K=1:10, H:K=2:10, H:K=4:10, H:K=6:10, corresponding to HNTs mass fractions of 0%, 9.1%, 16.7%, 28.6% and 37.5%, respectively.

Just Accepted



Scheme 1 (a) Schematic illustration of the preparation and mechanism of self-gelling HNTs/KGM sponges. Application of the HNTs/KGM sponges in (b) hemostasis and (c) wound healing.

2.3 Characterization

KGM, HNTs/KGM composite sponges, and HNTs were measured by Fourier-transform infrared spectroscopy (FT-IR) analysis (Bruker-TENSOR27, Germany) in the wavelength range of 400-4000 cm^{-1}. X-ray diffraction (XRD) analysis was performed to characterize the crystalline phases and structure of the samples. The measurements were conducted using a Rigaku Smartlab-9 kW diffractometer (Japan) operated at a tube voltage of 45 kV and a current of 200 mA. The surface topography of the composite sponges and the dispersion state of the HNTs were investigated via scanning electron microscopy (SEM). A Carl Zeiss Sigma 360 microscope (Germany), fitted with an energy spectrometer, was utilized for imaging at an accelerating voltage of 10 kV under high vacuum. To evaluate the mechanical properties under compressive loading, compression tests were performed on an electronic universal testing machine (CMT4503, MTS Systems (China) Co. Ltd.) at a speed of 2 mm/min.

2.4 Water absorption capability

Water uptake of HNTs/KGM sponges was measured by weighing before and after immersion [35]. The sponge was fully immersed in distilled water for 5 min to record its saturated weight. All tests were repeated three times. The water uptake ratio was calculated by Eq. (1):

$$Water\ absorption\ ratio = \frac{W_1 - W_0}{W_0} \times 100\% \quad (1)$$

where W_0 and W_1 are the dry and wet weights of the sponge, respectively.

Water absorption kinetics: 600 μL of water was added to the surface of a container, the HNTs/KGM sponge was placed on it. And the whole process was recorded on video (Movie S1).

2.5 Porosity measurements

Anhydrous ethanol was used to determine the porosity of the cylindrical sponges. For each dry sample, the mass, height, and diameter were measured with an analytical balance and a digital caliper; the bulk volume (V_0) was then derived from these data. Porosity testing was carried out by soaking each sponge in absolute ethanol (density ρ_0) for 5 min. After soaking, the sponge was taken out and its wet weight was recorded immediately. Porosity values were calculated using Eq. (2):

$$Porosity = \frac{W_1 - W_0}{\rho V_0} \times 100\% \quad (2)$$

where W_0 and W_1 are the weights of dry and saturated sponges, respectively [36].

2.6 Blood clotting index test

Blood clotting index (BCI) was measured following a published method [37]. A 5 mg piece of each sponge was put into a 40 mL glass vial. Then 200 μL citrated whole blood mixed with 20 μL $CaCl_2$ (0.2 M) was added onto the sample. The sample was left at room temperature for 5 min. After adding 8 mL of water, the mixture was centrifuged, and the absorbance of the supernatant was measured at 540 nm. A blank control group was included. Each test was run 5 times. BCI was calculated by the Eq. (3):

$$BCI = \frac{A_1}{A_0} \times 100\% \quad (3)$$

where A_1 refers to the sample absorbance, and A_0 to that of the blank control.

2.7 Whole blood clotting time test

Whole blood clotting time was measured using the test tube method described previously [38]. A 10 mg piece of each sponge was put into a tube. Then 400 μL blood and 40 μL $CaCl_2$ (0.2 M) were added. The tube was kept at 37°C. After 2 min, the tube was tilted gently at 20 s intervals until the cessation of blood flow was observed. The time when the clot no longer moved was taken as the clotting time. Each sample was tested five times.

2.8 Hemolysis assay

Hemolysis was tested using fresh whole blood which were washed with 0.9% NaCl and centrifuged. The washing step was repeated six times. The isolated red blood cells (RBCs) were then resuspended in 0.9% NaCl to make a 2%(v/v) RBCs suspension. For the test, each sponge was placed in a polypropylene tube. Then saline (2 mL) and 2% RBCs suspension (2 mL) were added. The tube was kept at 37°C for 1 h. Then it was spun down (3000 rpm, 10 min). The absorbance of the supernatant was read at 540 nm. Throughout the experiment, distilled water was adopted as the positive control, and physiological saline was correspondingly used as the negative control for comparison. The hemolysis rate (%) was calculated by Eq. (4):

$$Hemolysis\ ratio(\%) = \frac{OD_s - OD_{nc}}{OD_{pc} - OD_{nc}} \times 100\% \quad (4)$$

where OD_s, OD_{nc}, and OD_{pc} are the absorbance values of the sample, negative control, and positive control, respectively.

2.9 In vitro cytotoxicity assessment

Cell viability was measured with a Cell Counting Kit-8 (CCK-8) (Yeasen, China) following published protocols [39-41]. L929 mouse fibroblasts were used to test the cytotoxicity of the HNTs/KGM sponges. To prepare the extract, each sponge sample was placed in DMEM at concentrations of 1, 3, 5, 7, and 10 mg/mL. The mixture was kept at 37℃ in a 5% CO_2 incubator for 24 h. For the cell assay, L929 cells were seeded into 96-well plates and grown for 24 h under the same conditions (37℃, 5% CO_2). The culture medium was then removed and replaced with a mix of 100 μL fresh DMEM and 100 μL of the sample extract. After another 24 h, 20 μL of CCK-8 reagent was added to each well, and the cells were incubated for 2 h. Cell viability was then determined by reading the absorbance at 450 nm. The viability was calculated from Eq. (5):

$$Cell\ viaility = \frac{OD_{Sample} - OD_{Blank}}{OD_{Control} - OD_{Blank}} \times 100\% \quad (5)$$

2.10 Interaction between HNTs/KGM sponge and blood cells

2.10.1 RBCs adhesion

A 5 mg of the HNTs/KGM sponge was mixed with 100 μL of a 50% red blood cell suspension. The mixture was kept at 37℃ for 10 min. Then it was washed three times with saline. After washing, the sponge was resuspended in 5 mL of distilled water. The tube was placed in a 37℃ water bath for another 10 min. After that, the sponge was ground with a glass rod to release. The supernatant was collected and spun down. The absorbance of the supernatant was read at 540 nm. As a control, 100 μL of RBCs were lysed with 5 mL of distilled water. Each test was done three times. The RBCs adhesion ratio (%) was calculated by Eq. (6):

$$RBCs\ adhesion\ ratio\ (\%) = \frac{A_s}{A_c} \times 100\% \quad (6)$$

where A_s and A_c are the absorbance of the sample and the control, respectively.

Concurrently, sponges were washed, then fixed with 2.5% glutaraldehyde. After dehydration, the sample was examined under SEM (Hitachi Su-8100, Japan) to see the RBCs [1].

2.10.2 Partial thromboplastin time (PTT)

The PTT assay was carried out in accordance with YY/T 1911-2023, the Pharmaceutical Industry Standard of the People's Republic of China: Test Method for Blood Coagulation of Medical Devices, to evaluate the effect of the materials on the intrinsic coagulation pathway, and the detailed operation procedures are provided in the Supporting Information.

2.10.3 Platelet Count

Peripheral blood (18 mL) was collected via vacuum venipuncture from one healthy female volunteer and anticoagulated with 3.2% sodium citrate. For each assay, 5 mg sample was weighed into a 1.5 mL centrifuge tube, followed by addition of 0.4 mL anticoagulated whole blood to fully cover the material; untreated anticoagulated whole blood served as the blank control. All tubes (samples and controls, run in duplicate) were incubated at 37 °C for 60 min on a thermostatic shaker at 60 rpm. After incubation, 4 μL of 0.5 M EDTA was added to terminate the reaction, and the upper whole blood fraction was immediately analyzed on

Just Accepted

an automated hematology analyzer (BC-7500 C, Shenzhen Mindray Bio-Medical Electronics Co., Ltd., Shenzhen, China) for platelet counting.

2.11 In vivo hemostatic assay

In vivo hemostatic effect of the samples was tested using a mouse liver hemorrhage model [42, 43] and tail amputation model. In the liver hemorrhage model, Kunming mice (6–8 weeks old, 4 mice per group) were anesthetized with isoflurane. An abdominal cut was made, and the liver was exposed. Any serous fluid around the liver was gently wiped off with sterile gauze. A piece of filter paper was placed at the bottom of the liver. An X-shaped bleeding wound (wound length: 10 or 12 mm; depth: 2 mm) was created on the middle liver lobe with a scalpel. The sample was applied directly to the wound site, while no sample was applied in the control group. The time from placement to when bleeding fully stopped was recorded as the hemostasis time (Movie S2). Blood loss was measured by weighing the filter paper and sample before and after the test. For the tail amputation model, Institute of Cancer Research mice (6–8 weeks old, 4 mice per group) were anesthetized and immobilized. The tail was disinfected with iodophor, and a piece of filter paper was placed beneath the tail before transection at 3 cm from the tip. Once spontaneous bleeding started, the sample was applied to the wound, whereas no material was applied in the blank control group. Hemostasis time was recorded as the duration until bleeding completely ceased. Blood loss was quantified by weighing the filter paper and sample before and after the test. The entire hemostatic process was video-recorded for further analysis.

The animal experiments were carried out following the guidelines of the Lab of Animal Experimental Ethical Inspection of Dr.Can Biotechnology (Zhejiang) Co., Ltd. and were approved by the Lab of Animal Experimental Ethical Inspection of Dr.Can Biotechnology (Zhejiang) Co., Ltd. (Ethical code: DRK-202504230415).

2.12 Self-gelling and adhesion properties test

To test the rapid self-gelling or adhesion properties of HNTs/KGM sponge upon contact with liquids. Initially, the HNTs/KGM sponge was placed on the finger joints, and then the sponge was immersed in distilled water (Methylene Blue stained). After the sponges had sufficiently absorbed the water and gelled, the gel was adhered to the finger joints and then turned the finger joints to observe the adaptability and adhesion of the gel, as well as the integrity of the gel structure.

Tissue Adhesion Performance: To verify the adhesion performance of HNTs/KGM sponge after self-gelling, the adhesion performance of the gel was detected after contact with wet-tissues and object surfaces. Take a piece of fresh pigskin purchased from the local market, remove the grease, and cut it into a rectangular block (2 cm × 3 cm). After wetting the surface of the pigskin with distilled water (Methylene Blue stained), and then a HNTs/KGM sponge (Φ=16 mm, h=4 mm) was applied to the pigskin. A steel ruler was used to gently press the specimen for 10 s. The steel ruler was lifted to observe the adhesion between the pigskin and the steel ruler. The steel ruler with pigskin attached was suspended in air for 1 min to check whether the pigskin fell off spontaneously. Qualitative evaluations of tissue adhesion were performed using chicken organs, including the heart, liver, lung, and pigskin. Briefly, approximately 20 mg of a cylindrical HNTs/KGM gel was adhered on the steel ruler surface adhering, and the adhesion state was observed and photographed. Furthermore, objects of different materials were also used to detect the adhesion of HNTs/KGM gel, including plastic, steel, glass, and wood.

Lap Shear Test: First, preparing two pieces of fresh pigskin that are the same size (sized 2 cm × 6 cm). Then, the HNTs/KGM sponge was laid onto the pigskin surface wetted with distilled water (adhesion area of 1.8 cm × 2 cm) and pressed for 5min under a 1200 g weight for 3 min to allow full adhesion of the two pig-skin. The tests were carried out at a constant shear speed of 20 mm min-1 using a universal trial machine (CMT-100N, Huzhou Fanshun Instrument Co., Ltd., China) after fixing the two attached pigskin to the upper and under holders. KGM sponge was used as a control. HNTs/KGM sponge (H: K=6:10) was used as a experimental group. The shear adhesion strength was calculated by dividing the maximum stress by the area. The formula was exhibited as follows, where the F_{max} is the maximum shear force, W is the width of the gel surface, and L is the length of the gel surface. All experiments were performed at room temperature. Each test set contained five samples, and calculate the average value of the 5 samples. The shear strength was calculated by Eq. (7):

$$Shear\ strength\ (Pa) = \frac{F_{max}}{WL} \quad (7)$$

2.13 Rheological Test

Rheological tests were conducted on a Discovery HR-2 rotational rheometer (TA Instruments Inc., New Castle, DE, USA) at 30 ± 2 °C with a 25 mm parallel-plate geometry. Cylindrical samples (16 mm diameter, 6 mm thickness) with 400 μL of water were subjected to time sweep measurements at 1% strain and 1 Hz within the linear viscoelastic region over 6-600 s to assess the gel evolution behavior.

2.14 In vivo wound healing performance of the HNTs/KGM sponge

Male Institute of Cancer Research mice were anesthetized with isoflurane, shaved on the back, and subjected to a 10 mm-diameter round wound. For the control group, the wound was covered with sterile gauze. For the sample groups, the wounds were covered with the KGM sponge, the HNTs/KGM sponge (H:K=6:10), and the HNTs powder alone (n = 3 wounds per group). Rats were housed individually so that the healing process could be followed closely. Digital photos of the wounds were taken on days 0, 3, 5, 7, 11, and 14 after surgery. The wound dressings were changed on days 3, 7, and 11. On day 14, the animals were euthanized, and full-thickness skin samples were collected. Tissues were fixed in 4% paraformaldehyde, dehydrated with gradient ethanol, and embedded in paraffin wax. The paraffin-embedded samples were cut into 3-4 μm sections, deparaffinized in xylene, rehydrated, and stained with Hematoxylin and Eosin (H&E) and Masson's Trichrome. The sections were examined under an SD microscope. Wound closure was measured with Image J software, and the healing rate was calculated using Eq. (7):

$$Wound\ healing\ rate\ (\%) = \frac{S_0 - S_N}{S_0} \times 100\% \quad (8)$$

where S_0 stands for the initial wound area on day 0, and S_N denotes the wound area measured on day N.

2.15 Statistical analysis

Just Accepted

All data are presented as mean ± SD. Statistical analysis was carried out with SPSS 19.0. One-way ANOVA accompanied by Dunnett's two-sided t-test was used for three or more group comparisons. Independent samples t-test was applied to compare differences between the two groups. All measurements were repeated three times unless specified otherwise. A p value less than 0.05 ($p < 0.05$) was regarded as statistically significant in all evaluations (*$p < 0.05$, **$p < 0.01$, and ***$p < 0.001$).

3 Results and discussion

3.1 Synthesis and characterization of HNTs/KGM Sponge morphology and composition

The KGM-based sponge was fabricated via the compounding of KGM with HNTs. A systematic investigation was conducted to characterize the microstructure and composition of the resulting HNTs/KGM composite sponges. SEM analysis revealed the morphological features of the sponges across varying HNTs levels (Fig. 1a). The pure KGM sponge exhibited a highly porous, interconnected network structure composed of thin, sheet-like layers. Upon the incorporation of HNTs, this porous architecture was largely preserved, though the layers became progressively thicker and the overall structure denser. At the highest HNTs ratio (H:K=6:10), localized signs of partial pore collapse were observed in certain regions. High-magnification SEM images confirmed that HNTs formed distinct aggregates that were effectively embedded within and distributed across the surface of the KGM matrix sheets. The density of these aggregates increased proportionally with the HNTs content. To confirm the identity of these structures, energy-dispersive X-ray spectroscopy (EDS) analysis was performed. The elemental maps for Al and Si [22], the primary constituents of HNTs, precisely co-localized with the observed aggregates, thereby verifying the successful and uniform incorporation of HNTs into the KGM framework (Fig. 1b).

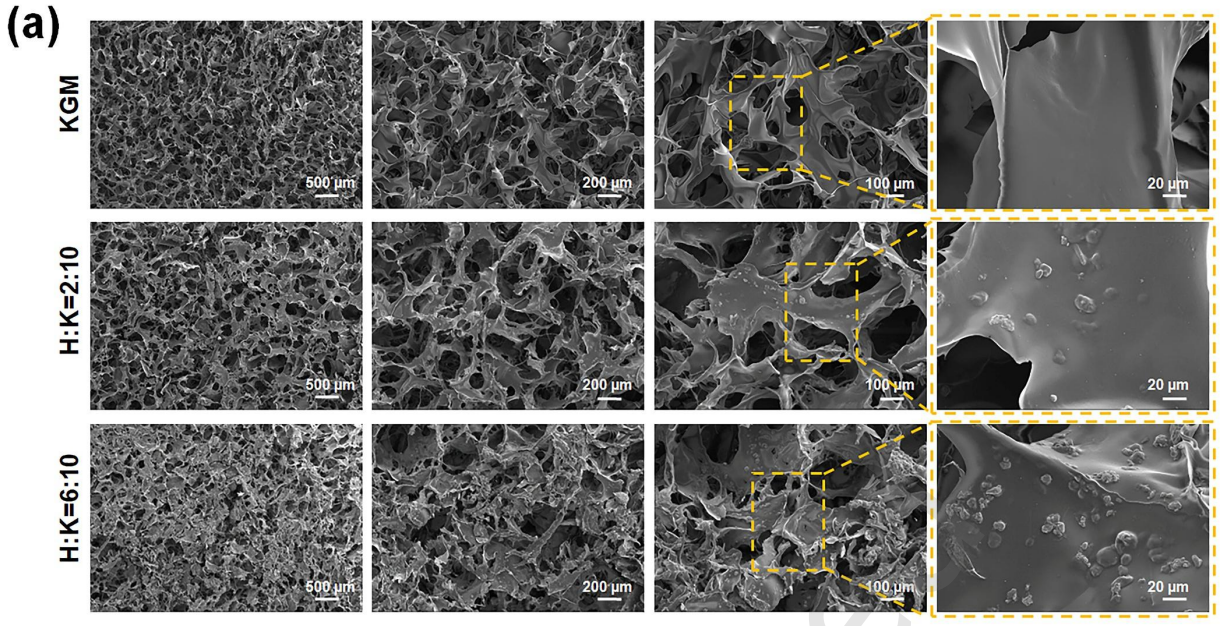
To further investigate the chemical composition and intermolecular interactions, FTIR and XRD analyses were conducted. The FTIR spectra (Fig. 1c) confirmed the presence of both components in the composite sponges. The spectrum for pure KGM displayed characteristic peaks corresponding to O-H stretching (3428 cm^{-1}), -CH_3 vibrations (2925 cm^{-1}), and C=O stretching from residual acetyl groups (1730 cm^{-1}) [28, 44]. With the addition of HNTs, new absorption peaks emerged that are characteristic of the clay mineral appeared, including inner-surface -OH stretching (3694 and 3623 cm^{-1}) and Si-O-Si stretching (1029 cm^{-1}) [9, 45]. The spectra of the HNTs/KGM composites represented a superposition of the individual components' spectra, with the intensity of HNTs-related peaks increasing with their concentration. Compared with pure HNTs, the O-H stretching vibration bands of the HNTs/KGM composite sponge exhibited slight shifts from 3694 cm^{-1} to 3696 cm^{-1} and from 3623 cm^{-1} to 3619 cm^{-1}, accompanied by an obvious peak broadening, which might be attributable to the hydrogen-bonding interactions between the hydroxyl groups of KGM and those on the HNTs surface [9].

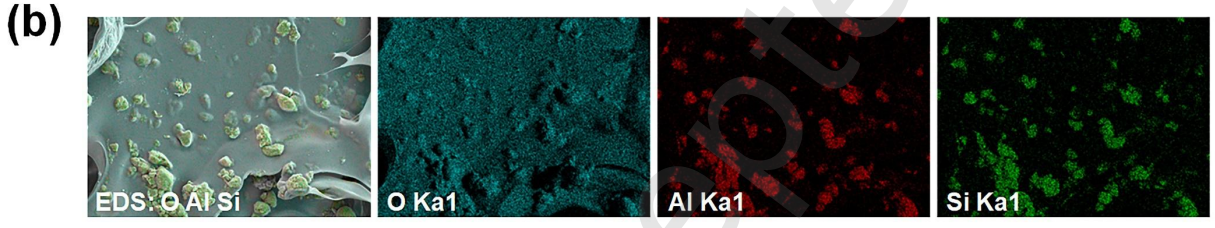
The crystalline nature of the sponges was assessed via XRD analysis (Fig. 1d). The pure KGM sponge exhibited a single broad diffraction hump centered at 22.2°, characteristic of its amorphous polymeric structure [46]. In contrast, pristine HNTs displayed a series of sharp diffraction peaks (e.g., 11.94°, 19.92°, 24.74°), confirming their well-defined crystalline nature (JCPDS No. 09-0453). In the composite HNTs/KGM sponges, both the amorphous diffraction hump from KGM and the crystalline peaks from HNTs were present. The intensity of the HNTs diffraction peaks progressively strengthened progressively with increasing HNTs content, providing further evidence for the successful incorporation of the crystalline clay filler into the amorphous polymer matrix.

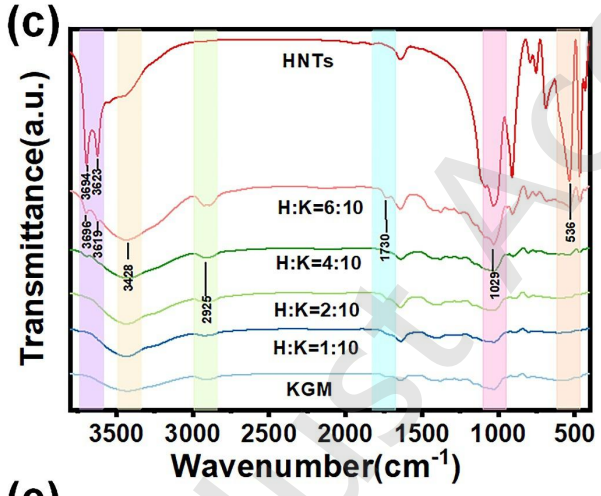
The mechanical properties of the sponges were characterized through compression testing (Fig. 1e-f). The stress-strain curves for all formulations exhibited the typical three-stage compression behavior characteristic of porous foam materials: an initial linear elastic region, a long plateau region corresponding to pore collapse, and a final densification stage. While the compressive strength remained consistent at approximately 0.09 MPa across all formulations regardless of HNTs content, the compressive modulus demonstrated a clear increasing trend (Fig. 1f). The modulus increased from 0.04 MPa for the pure KGM sponge to 0.105 MPa for the composite with the highest HNTs loading (H:K=6:10). This indicates that the incorporation of rigid HNTs particles effectively reinforces the KGM matrix, enhancing its stiffness without compromising the overall structural integrity under compression.

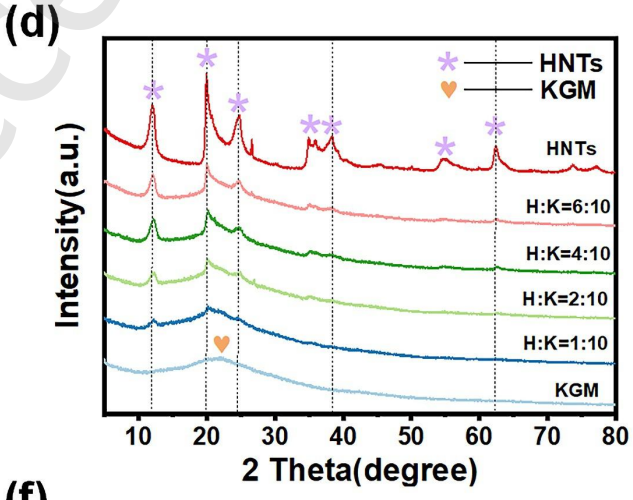
Furthermore, HNTs/KGM sponges possessed certain compressive shape recovery capacity, and the incorporation of HNTs exerted no significant effect on the shape recovery performance of the sponges. The shape recovery ratio of HNTs/KGM sponges reached approximately 85% upon 30% compression, and decreased to around 45% after 70% compression (Fig. S3). The gelled sponges exhibited no compressive shape recovery capability (Fig. S4).

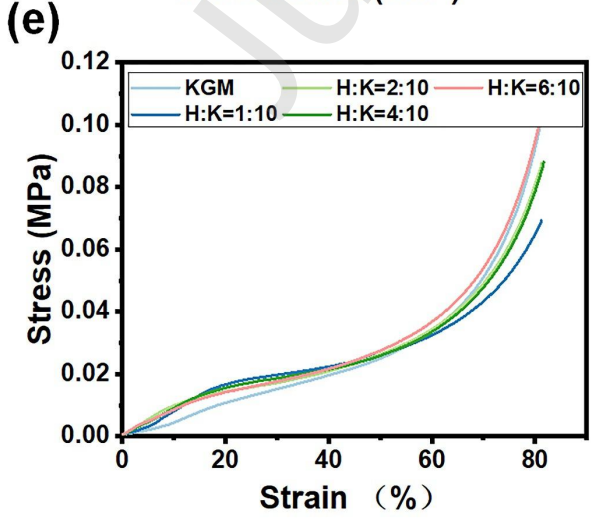
Just Accepted

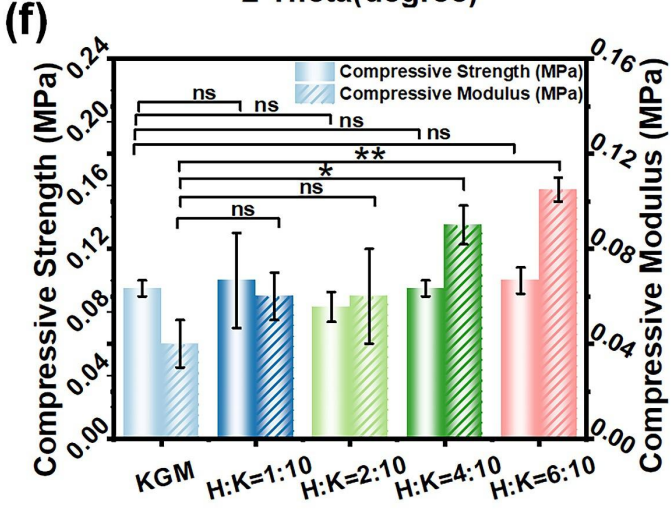












Just Accepted

Figure 1 Characterization. (a) SEM images of HNTs/KGM sponges with varying HNTs ratios. (b) Mapping images of O, Al, and Si elements of HNTs/KGM sponge (H: K=6:10). (c) FTIR spectra and (d) XRD patterns of HNTs/KGM sponges with different blend ratios and HNTs. (e) The stress-strain curves and (f) the compressive performance of HNTs/KGM sponges with varying HNTs ratios. *p < 0.05, **p < 0.01, ***p < 0.001.

3.2 In vitro biocompatibility and hemocompatibility

The clinical translation of any hemostatic agent is dependent on its biocompatibility [3]. To ensure the safety of the HNTs/KGM sponges, we systematically assessed their biocompatibility through standardized in vitro cytotoxicity and hemolysis assays.

The cytocompatibility of the material was evaluated using L929 fibroblasts, a widely recognized cell line for biomaterial testing. Following a 24 h incubation with material extracts, microscopic examination revealed that L929 cells retained a healthy, spindle-like morphology across all test groups, with no discernible differences from the control group (Fig. 2a and Fig. S1). This qualitative observation was corroborated by a CCK-8 cell viability assay (Fig. 2b). The cell viability for all HNTs/KGM sponge groups exceeded 95%, well within the non-cytotoxic range as defined by ISO 10993-5 standards [47]. Although the highest concentration of pure HNTs extract exhibited a minor decrease in viability, it remained above the safety threshold, confirming the overall cytocompatibility of the composite material.

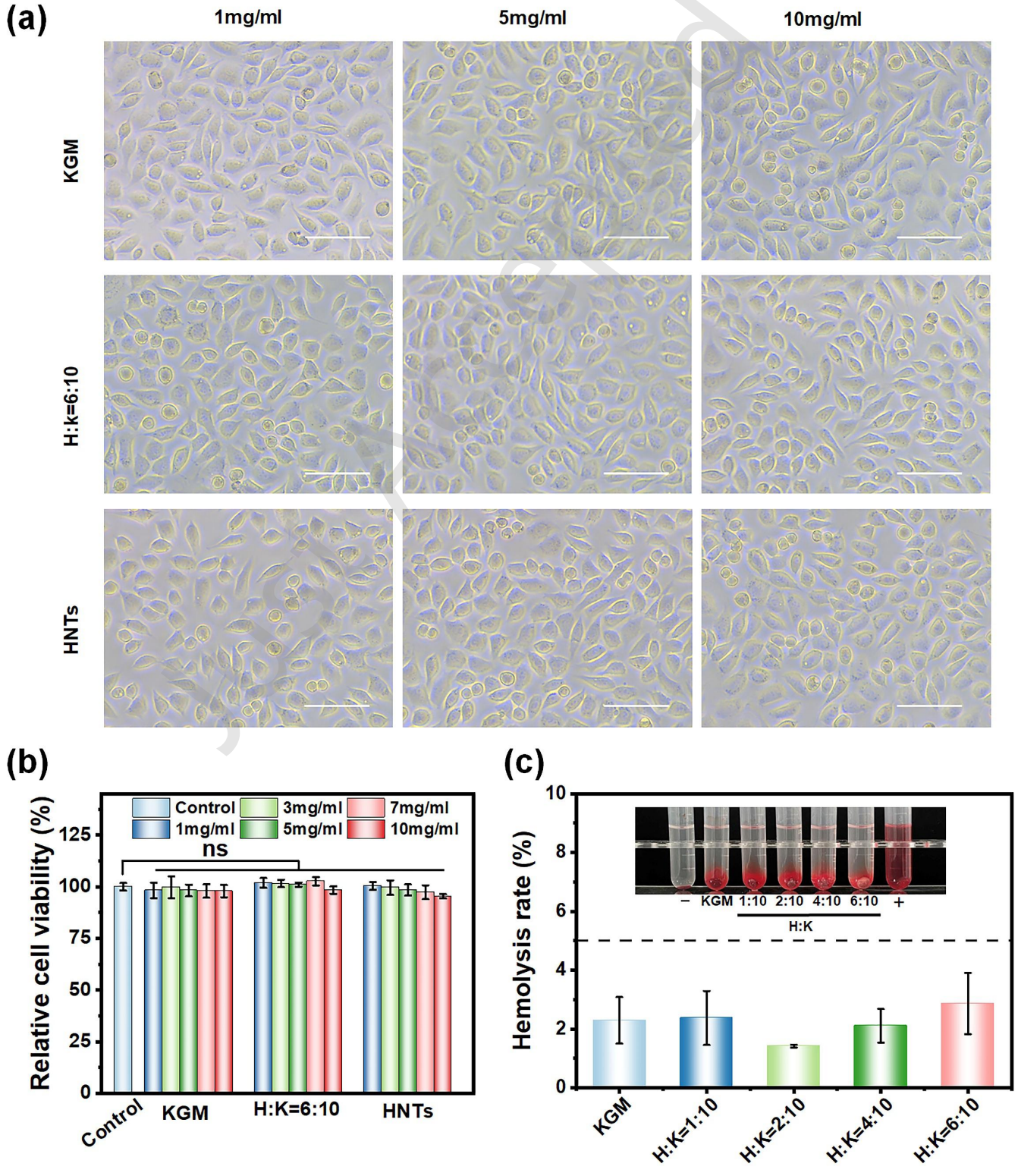


Figure 2 Biocompatibility. (a) Optical microscope images of L929 fibroblasts incubated with KGM, HNTs/KGM sponge (H:K=6:10) and HNTs. Scale bars, 100 μm. (b) Cytotoxicity of KGM, HNTs/KGM sponge (H:K=6:10) and HNTs. (c) Hemolysis assays and hemolysis images (insert) of RBCs incubated with KGM and HNTs/KGM sponges. *p < 0.05, **p < 0.01, ***p < 0.001.

To evaluate blood compatibility, a critical parameter intended for materials designed for blood contact [48], a hemolysis assay was performed (Fig. 2c). Visually, the supernatants of all sponge-treated groups remained clear and transparent, with no evidence of red blood cell lysis and were distinguishable from identical to the negative control (saline). In contrast, the positive control (distilled water) exhibited complete hemolysis, as evidenced by its bright red coloration. The measured hemolysis rates for all HNTs/KGM sponge formulations were well below the internationally accepted safety threshold of 5%.

These findings collectively demonstrate that the HNTs/KGM sponges exhibit excellent biocompatibility. They are non-cytotoxic and highly hemocompatible, indicating that the material can be safely utilized in direct contact with tissues and blood. This favorable safety profile is a fundamental prerequisite for its application as a hemostatic agent and suggests it can provide an appropriate microenvironment conducive to subsequent wound healing.

3.3 Self-gelling, wet-tissue adhesion, and mechanical resilience of the HNTs/KGM sponge

For effective management of irregular bleeding, an ideal hemostatic agent must be capable of forming a stable gel in situ, exhibiting tenacious adhesion to wet and bleeding tissues, and possessing sufficient the mechanical flexibility to conform to irregular wound cavities [49-52]. To evaluate the functional properties of the HNTs/KGM sponges, we assessed their self-gelling behavior, wet-adhesive adhesion, conformability, and adhesion strength (Fig. 3).

Just Accepted

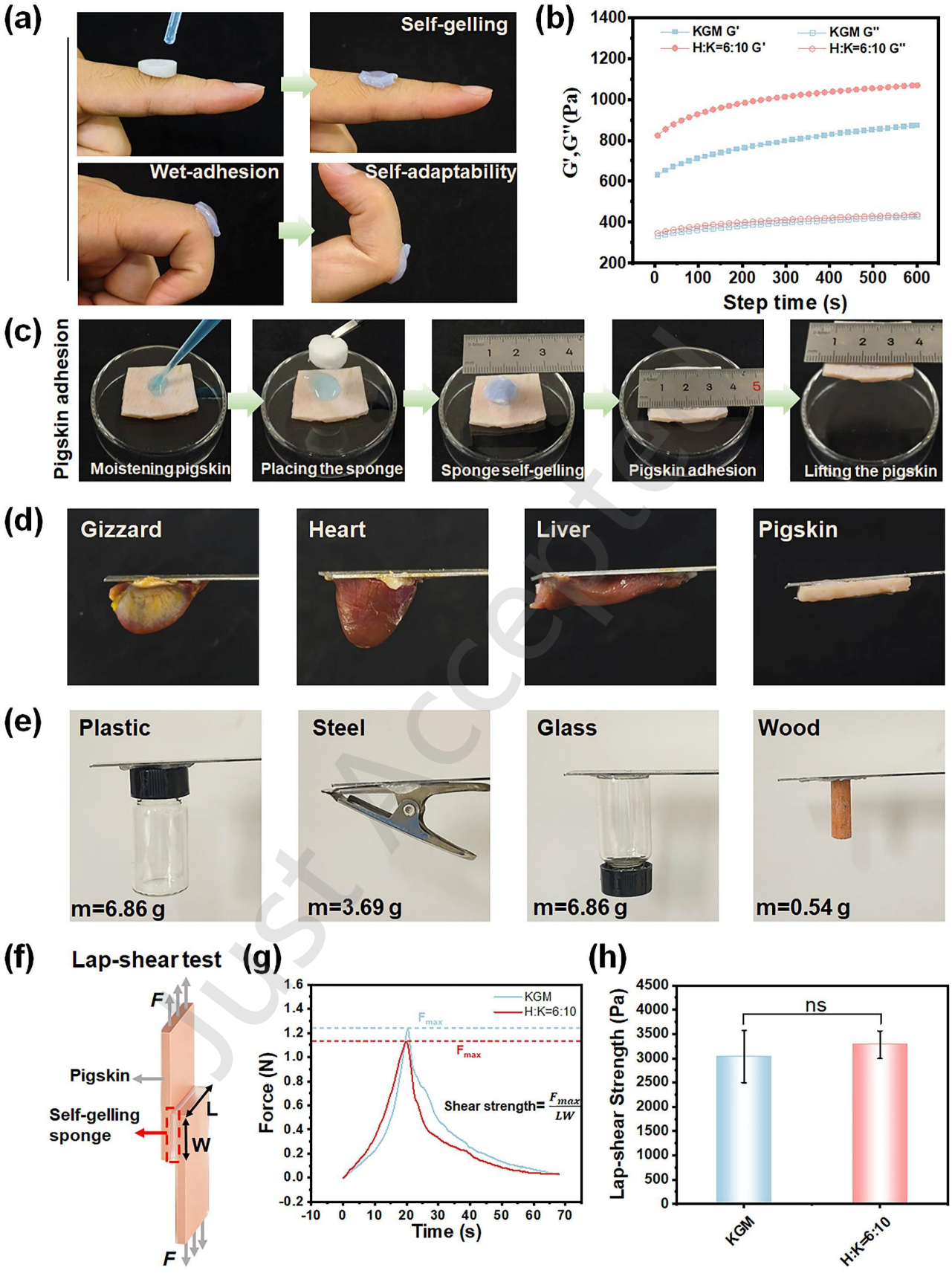


Figure 3 Self-gelling of HNTs/KGM sponge, rheological behavior, wet-adhesive performance, shape adaptability after gelation and adhesion strength. (a) Self-gelling, the adhesion capacity and the self-adaptability of HNTs/KGM sponge (H:K=6:10). (b) Rheological behavior of gels in time scanning mode. (c) Photographs of HNTs/KGM sponge (H:K=6:10) undergoing self-gelling and wet-adhesion processes between wet tissues. (d) Photographs of HNTs/KGM gel (H:K=6:10) adhered to fresh organs or tissues and (e) substrates. (f) Schematic illustration of the Lap-shear test. (g) Representative time-stress curves of the Lap-shear test. (h) Lap-shear strength of fibrin glue and HNTs/KGM gel (H:K=6:10, n = 5). *p < 0.05, **p < 0.01, ***p < 0.001.

Just Accepted

A distinctive feature of the HNTs/KGM sponge is its ability to undergo rapid, in situ gelation upon contact with aqueous fluids. Qualitative observations revealed that the dry sponge rapidly transformed into a cohesive hydrogel upon hydration, enabling it to adhere firmly to skin (Fig. 3a). Beyond its adhesive properties, the hydrogel exhibited excellent flexibility and conformability. When applied to a dynamic joint such as a finger, the gel maintained both its structural integrity and adhesion throughout repeated bending and straightening motions (Fig. 3a). This high degree of deformability is particularly advantageous for irregular wound applications, as it suggests the material can effectively conform to and seal deep, irregularly shaped wounds without fracturing or dislodging. The hydrogel's solid-like viscoelasticity is confirmed by time sweep tests (Fig. 3b): storage modulus (G') remains higher than loss modulus (G") throughout the entire test period, and the H:K=6:10 sample exhibits a higher G' than pure KGM, demonstrating the strengthening effect of HNTs on the gel.

This gelation process is accompanied by robust wet-tissue adhesion, a critical property for effectively sealing wounds against blood flow [53]. Fig. 3c illustrated the wet adhesion behavior of HNTs/KGM sponges between a steel ruler and porcine skin after self-gelation. The sponge was sandwiched between the steel ruler and hydrated porcine skin for 10 s. Gentle lifting of the steel ruler elevated the porcine skin together, confirming that the HNTs/KGM sponge converted into an adhesive hydrogel and bonded tightly with tissues. In addition, the adhesion performance of the HNTs/KGM hydrogel against wet tissues was further evaluated. Adhesion tests demonstrated that the formed hydrogel displayed robust adhesion when applied to fresh wet tissues (heart, liver, spleen and porcine skin), and the material could bear its own weight after attachment (Fig. 3d).

This adhesive capability extended to various substrates, including plastic, steel, glass, and wood (Fig. 3e). In this study, freshly obtained pig skin, which exhibits mechanical properties analogous to human skin, was employed as a model to assess the shear adhesion performance of the hydrogels, as illustrated in Fig. 3f-h. The bonding strengths of pure KGM hydrogel and HNTs/KGM composite hydrogel were 3037 Pa and 3281 Pa, respectively (Fig. 3h). The results indicated that both materials exhibited favorable adhesion performance. The adhesive mechanism can be attributed to the inherent characteristics of the KGM matrix. Abundant hydroxyl groups and other hydrophilic moieties of KGM interact with water molecules via hydrogen bonds and van der Waals forces. These functional groups form effective interactions with the moisture on the skin surface, which improves the adhesion capacity and enables rapid and stable anchoring on biological tissues [1, 31, 34].

3.4 In vitro hemostatic performance: a dual-mode mechanism

To evaluate the hemostatic potential of the HNTs/KGM sponges, we conducted their performance through a series of in vitro assays to assess both their physical properties conducive to hemostasis (liquid absorption capacity and porosity) and their direct biochemical effects on blood coagulation (whole blood clotting time and blood clotting index).

A primary physical mechanism underlying hemostasis involves the rapid concentration of blood components at the wound site. The HNTs/KGM sponges exhibited superior liquid absorption properties (Fig. 4a-b). All composite sponges became fully hydrated and formed compact hydrogels within 1 s (Fig. 4a and Movie S1), which reflected their strong hydrophilicity. While the incorporation of HNTs slightly modulated the total capacity, all composite sponges retained highly absorption properties. The water uptake ratio of the pure KGM sponge was 3625 ± 343%, and even the composite with the highest HNTs loading (H:K=6:10) maintained a capacity of 2089 ± 153% (Fig. 4b). Notably, this surpasses conventional hemostatic agents such as gauze (819%) and oxidized regenerated cellulose (278%) [54, 55]. This high absorptivity is attributed to the sponge's high porosity (~95%), which remained consistent across all formulations (Fig. 4c), ensuring ample surface area for blood interaction and concentration.

Beyond physical absorption, we evaluated the sponges' ability to actively induce the coagulation cascade through whole blood clotting assays (Fig. 4d-e). The whole blood clotting time decreased significantly with increasing HNTs content. Pure KGM alone did not significantly shorten clotting time compared to the blank control (536 s vs. 584 s; $p > 0.05$), indicating limited intrinsic pro-coagulant activity. In contrast, the integration of HNTs markedly accelerated coagulation. The clotting time for the H:K=6:10 composite sponge was reduced to 325 ± 17 s, significantly faster than KGM alone ($p < 0.001$) and approaching the efficacy of pure HNTs powder (205 ± 12 s). This confirms that the potent pro-coagulant activity is mediated by the HNTs component.

These findings were corroborated by the blood clotting index (BCI), where a lower value indicates more effective clotting (Fig. 4e). The BCI for the H:K=6:10 sponge (9.09 ± 2.01%) was drastically lower than the blank control (62.03 ± 1.64%) and the pure KGM sponge (25.52 ± 3.76%), and was comparable to pure HNTs powder. The moderate BCI reduction by the pure KGM sponge can be ascribed to its porous architecture facilitating red blood cell adhesion, while the dramatic decrease in the composites is clearly due to the biochemical activation of the coagulation cascade by HNTs. In conclusion, the HNTs/KGM sponges employ a potent dual-mode hemostatic mechanism. First, the highly porous KGM matrix functions as a physical concentrator, rapidly absorbing blood plasma to localize platelets and clotting factors [31]. Concurrently, the embedded HNTs provide a high-density, charged surface that actively accelerates the intrinsic coagulation pathway [11]. This synergistic integration of physical concentration and biochemical activation positions the HNTs/KGM sponge as a highly effective hemostatic agent.

Notably, KGM exhibits superior coagulation performance in the early stage of coagulation. At 1 min, the clotting index of pure KGM is 21.5%, considerably lower than the value of 83.4% for pure HNTs (Fig. S2a). Additionally, the hemostatic capacity of the material is directly correlated with sample dosage. At the same time point of 1 min, the clotting index of 20 mg KGM is much lower than that of 5 mg KGM, reaching only 3.3% (Fig. S2b).

Just Accepted

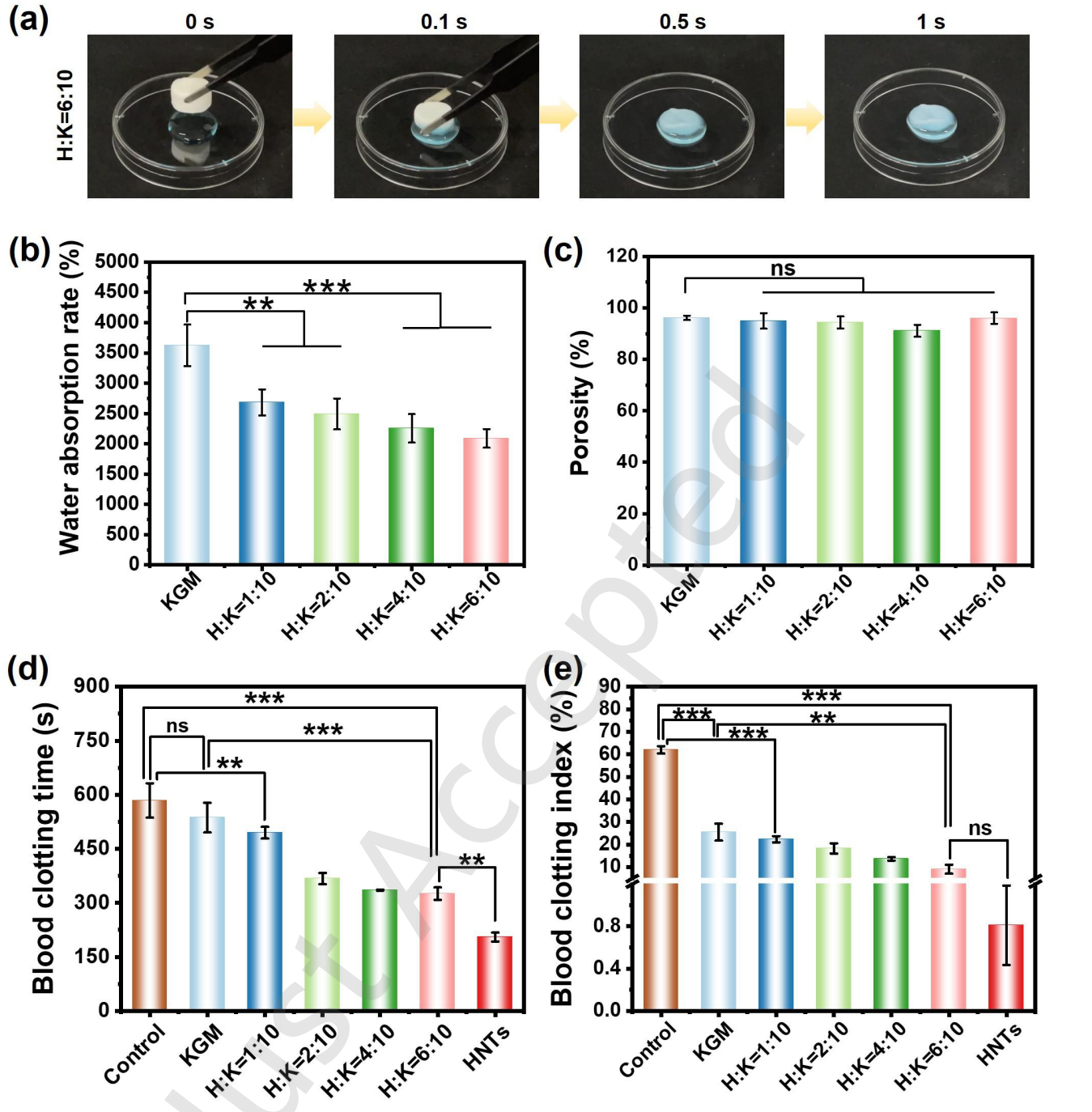


Figure 4 In vitro blood coagulation analysis. (a) Photographs showing the water absorption process of HNTs/KGM (H:K=6:10) sponges. (b) Water absorption rate and (c) Porosity of HNTs/KGM sponges with varying HNTs ratios. (d) Whole blood clotting time and (e) Blood clotting index of HNTs/KGM sponges with varying HNTs ratios and HNTs (5 min). *p < 0.05, **p < 0.01, ***p < 0.001.

Just Accepted

3.5 Mechanistic insights into the dual-action hemostatic function

To elucidate the mechanism underlying the potent hemostatic performance of the HNTs/KGM sponge, we performed a comprehensive investigation into its interactions with critical blood components, namely red blood cells RBCs. Our findings reveal a synergistic, dual-action mechanism that integrates rapid physical entrapment with potent biochemical coagulation.

The HNTs/KGM composite exhibits its primary physical action through the rapid aggregation and firm immobilization of RBCs, driven by the porous and hydrophilic KGM matrix [31]. This phenomenon was initially demonstrated in a qualitative RBC adhesion assay (Fig. 5a). Upon exposure to saline, the HNTs/KGM hydrogels demonstrated remarkable tension dense population of RBCs, in contrast to the near- complete washout observed with the pure HNTs powder. Quantitative analysis corroborated this observation, with all HNTs/KGM composite sponges achieving over 90% RBC adhesion, compared to HNTs powder retained a negligible 0.16% for the HNTs powder alone (Fig. 5b). SEM provided visual confirmation, revealing extensive entrapment and immobilization of RBCs within the interconnected KGM hydrogel (Fig. 5c). This efficient physical trapping mechanism concentrates blood cells at the injury site, forming a primary, physical barrier and increasing local blood viscosity [3, 56].

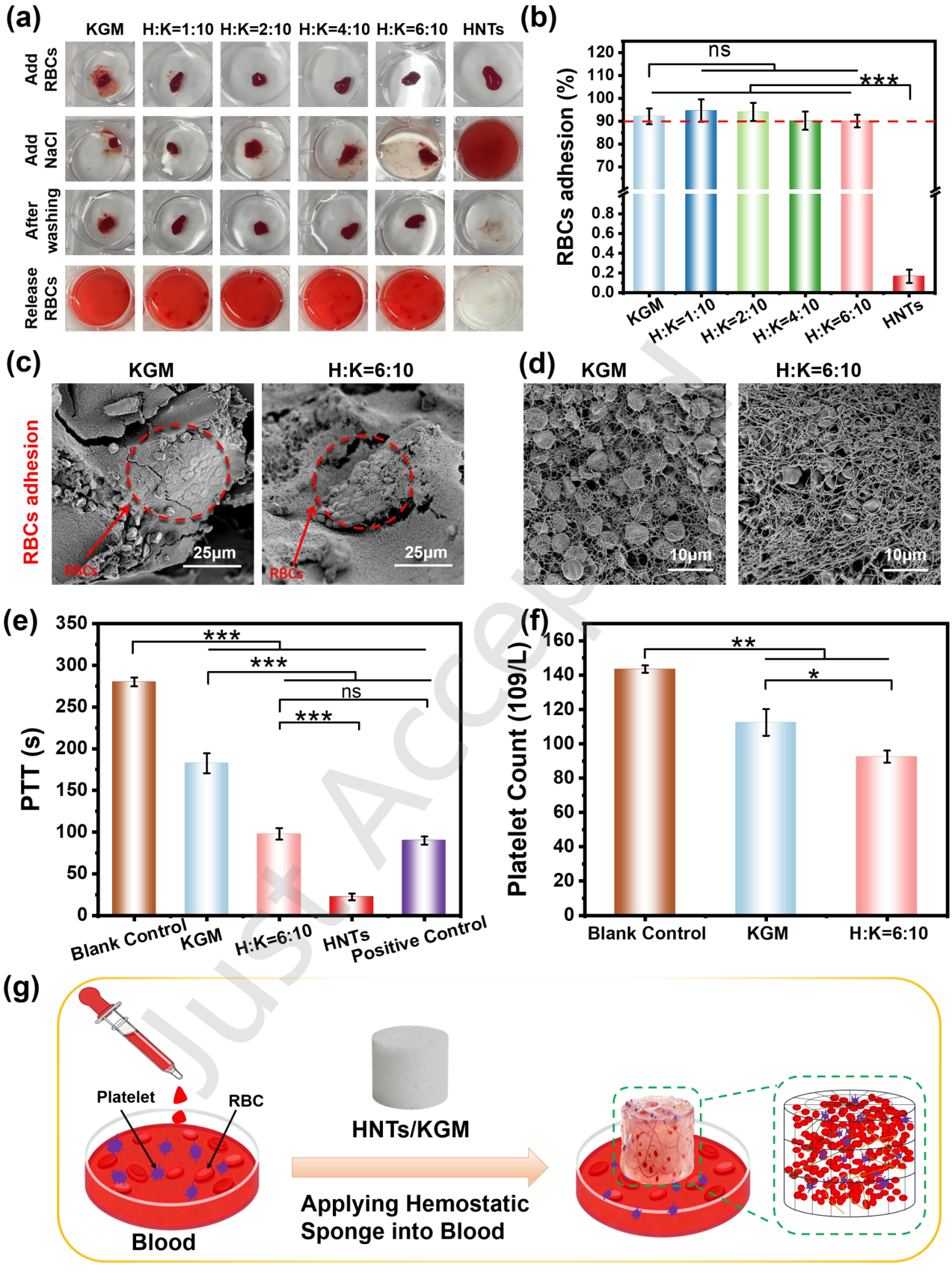


Figure 5 Analysis of RBC and platelet adhesion ability and hemostatic mechanism of HNTs/KGM sponges. (a) Photographs showing the experimentation of HNTs/KGM sponges with varying HNTs ratios and HNTs. (b) RBC adhesion (%) of HNTs and HNTs/KGM sponges with varying HNTs ratios. (c) Representative SEM images of RBCs adhering to KGM and HNTs/KGM sponges (H:K=6:10). (d) Representative SEM images of blood cells enwrapped by fibrin networks. (e) PTT of HNTs, KGM and HNTs/KGM sponges (H:K=6:10). (f) Platelet count of KGM and HNTs/KGM sponges (H:K=6:10). (i) Schematic illustration of the pro-coagulant mechanism of the HNTs/KGM sponge. *p < 0.05, **p < 0.01, ***p < 0.001.

Just Accepted

SEM analysis of KGM and H:K=6:10 sponges exposed to whole blood revealed abundant fibrin filaments on their surfaces (Fig. 5d), with blood cells tightly encapsulated within the fibrin network. The fibrin network of the H:K=6:10 composite sponge exhibited higher density. This phenomenon can be mainly attributed to the negatively charged surface of HNTs, which activates the intrinsic coagulation pathway (Fig. 5e) [6, 11] and accelerates the conversion of fibrinogen to fibrin, thereby crosslinking and immobilizing the entrapped red blood cells [57]. Furthermore, the H:K=6:10 sponge exhibited a greater reduction in platelets relative to the KGM sponge (Fig. 5f), suggesting enhanced platelet adhesion, which is beneficial for hemostasis.

In summary, the superior hemostatic efficacy of the HNTs/KGM sponge is attributed to the physical absorption and the activation of the intrinsic coagulation pathway, as illustrated in Fig. 5g. Upon contact with blood, the highly porous KGM matrix and HNTs rapidly absorb blood, concentrating and physically entrapping large numbers of RBCs and platelets, while activating the intrinsic coagulation pathway to promote fibrin generation, thereby accelerating the coagulation process.

3.6 In vivo hemostatic efficacy and operability in a irregular hemorrhage model

Given its superior in vitro performance, the HNTs/KGM sponge with the highest HNTs loading (H:K=6:10) was evaluated in an in vivo mouse liver hemorrhage model (Fig. 6a) and tail amputation model (Fig. 6e). Its hemostatic performances in liver injury and tail amputation models were compared with a blank control (no treatment), commercial gauze, KGM sponge and pure HNTs powder.

In the liver hemorrhage model, the H:K = 6:10 sponge exhibited outstanding hemostatic performance, achieving hemostasis within 152.50 ± 19.53 s with a total blood loss of only 76.65 ± 11.84 mg (Fig. 6b–d). Compared with the blank control group, it reduced the bleeding time by 29.89% and blood loss by 75.24%. Relative to the KGM sponge group (151.25 ± 27.24 s; 107.15 ± 3.14 mg), the H:K = 6:10 sponge decreased blood loss by 28.47%. Furthermore, both the KGM sponge and H:K = 6:10 sponge exhibited markedly superior hemostatic performance compared with gauze (207.50 ± 10.31 s; 229.45 ± 19.42 mg).

Notably, in the liver model with milder trauma (wound length: 10 mm; depth: 2 mm), both the KGM sponge and H:K = 6:10 sponge yielded significantly shorter bleeding time and lower blood loss than the blank control group (Fig. S5). However, no significant difference was observed between the KGM sponge and H:K = 6:10 sponge. In addition, their blood loss was only slightly different from that of the gauze group. It is speculated that the hemostatic function of HNTs cannot be fully exerted in the hemostasis model with a relatively short hemostatic time (approximately 110 s), which is consistent with the results of the whole blood coagulation test.

The effects of the HNTs/KGM sponge on blood loss and hemostasis time were also investigated in the mouse tail amputation model. Similarly, compared with the blank control group (77.45 ± 12.71 mg; 199.50 ± 21.70 s), the H:K=6:10 sponge group and the KGM group exhibited superior hemostatic efficacy (Fig. 6f–h). Their blood loss values were 1.73 ± 0.29 mg and 4.97 ± 1.01 mg, representing reductions of 97.77% and 93.58%, respectively. Meanwhile, shorter hemostatic times of 46.25 ± 10.08 s and 47.00 ± 10.70 s were achieved, corresponding to reductions of 76.82% and 76.44%, respectively (Fig. 6g, h). In addition, both the H:K=6:10 sponge group and the KGM group showed significantly better hemostasis than the gauze group (32.02 ± 6.70 mg; 188.75 ± 7.40 s). To explore the effect of halloysite on the hemostatic performance of KGM, supplementary statistical analysis of blood loss was performed among the H:K=6:10 sponge group and KGM group (Fig. S6). The blood loss of the H:K=6:10 sponge group was significantly lower than that of the KGM group, which was consistent with the in vitro coagulation results.

Beyond hemostatic efficacy, the composite sponge addressed a key clinical challenge associated with powdered hemostats: operability and ease of removal (Fig. 6i). Following hemostasis, the HNTs/KGM sponge could be cleanly removed as a single, intact from the wound site. In contrast, the HNTs powder left significant residue adhered to the liver tissue, which is difficult to clean and may pose risks of inflammation or embolism. This demonstrates that the KGM matrix not only provides adhesion and flexibility but also successfully encapsulates the HNTs, preventing secondary complications and showcasing a distinct advantage for clinical translation.

Just Accepted

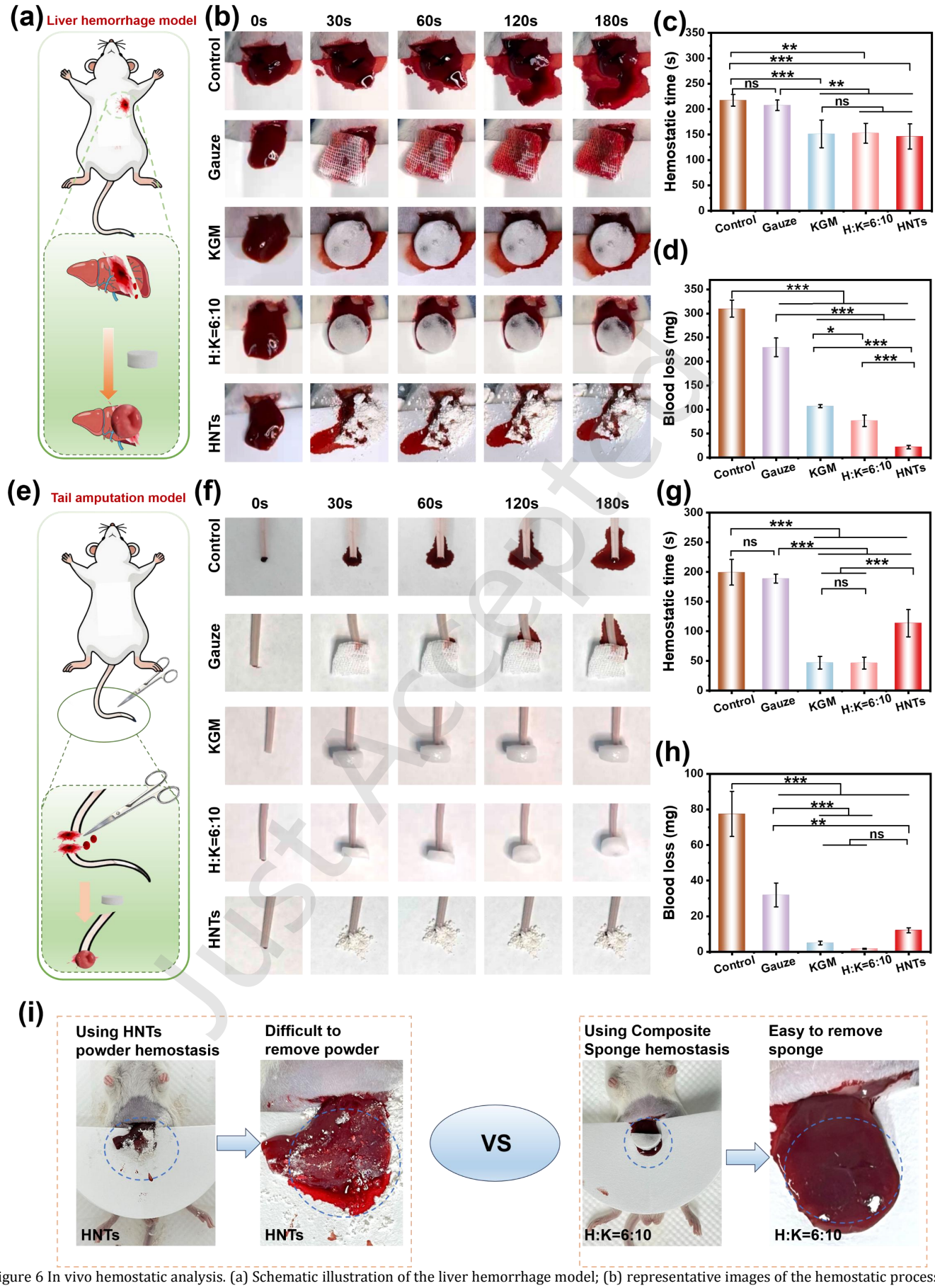


Figure 6 In vivo hemostatic analysis. (a) Schematic illustration of the liver hemorrhage model; (b) representative images of the hemostatic process, (c) hemostatic time and (d) relative blood loss for the liver hemorrhage model (wound length: 12 mm; depth: 2 mm) treated with sterile gauze, KGM sponge, HNTs/KGM sponge (H:K=6:10), and HNTs. (e) Schematic illustration of the tail amputation model; (f) representative images of the hemostatic process, (g) hemostatic time and (h) relative blood loss for the tail amputation model treated with sterile gauze, KGM sponge, HNTs/KGM sponge

Just Accepted

(H:K=6:10), and HNTs. (i) Photographs showing easy removal of samples in the milder liver hemorrhage model (wound length: 10 mm; depth: 2 mm). *p < 0.05, **p < 0.01, ***p < 0.001.

3.7 Study on wound healing of the HNTs/KGM sponge in vivo

The rapid and effective closure of injured skin not only safeguards the internal milieu but also creates a moist physiological environment that favors wound healing. [58, 59]. The results of this study demonstrate that the developed HNTs/KGM sponge exhibits multiple wound-healing properties, including gelation capability, high water-retention capacity, wet adhesion property, self-adaptability and excellent biocompatibility, showing great potential in wound care. Full-thickness skin wounds on the backs of rats were treated to treatment with various hemostatic materials over 14-day period, with careful documentation of wound healing progression (Fig. 7a). The control group wounds were treated with sterile gauze, serving as the blank control. The experimental groups received applications of KGM sponge, HNTs/KGM sponge (H:K=6:10), and HNTs powder, respectively. Wound conditions were monitored on days 0, 3, 5, 7, 11, and 14 (Fig. 7b).

Just Accepted

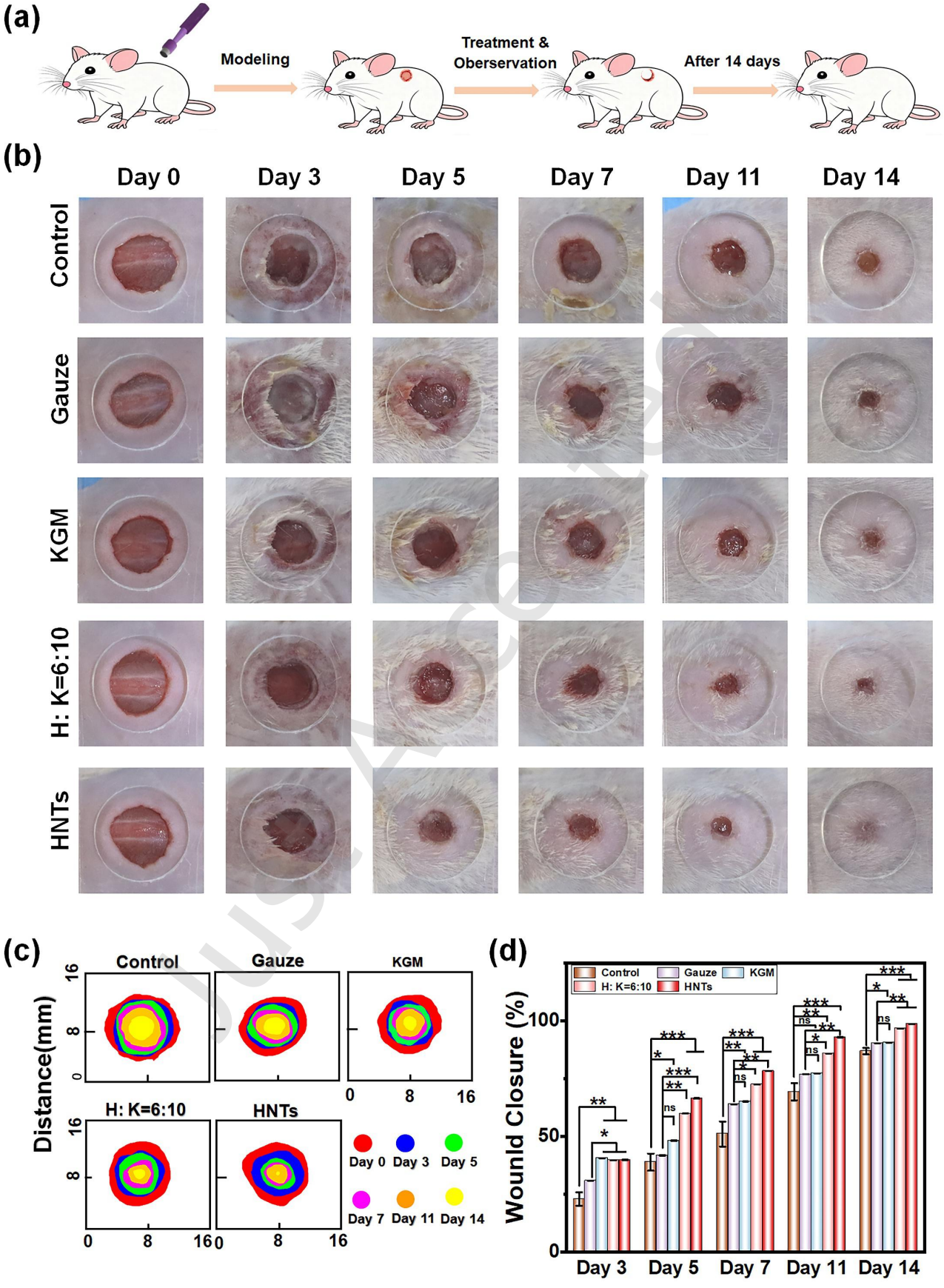

(a)
Modeling
Treatment & Oberservation
After 14 days
(b)
Day 0
Day 3
Day 5
Day 7
Day 11
Day 14
Control
Gauze
KGM
H: K=6:10
HNTs
(c)
Control
Gauze
KGM
H: K=6:10
HNTs
Distance(mm)
Day 0 Day 3 Day 5
Day 7 Day 11 Day 14
(d)
Control
Gauze
KGM
H: K=6:10
HNTs
Wounld Closure (%)
Day 3
Day 5
Day 7
Day 11
Day 14

Figure 7 Wound healing performance of different hemostatic materials. (a) Schematic diagram and (b) representative images of wound healing. (c) Schematic diagram of dynamic wound healing. (d) Quantitative data of relative wound area at different time points. *p < 0.05, **p < 0.01, ***p < 0.001.

As displayed in Figure 7b, by day 7, the wound areas in the HNTs/KGM sponge (H:K=6:10) group and the HNTs group were significantly smaller than those in the gauze group and the control group. By day 14, most wounds in the HNTs/KGM sponge (H:K=6:10) group and the HNTs group had fully healed, while significant non-healing was still observed in the KGM group, the gauze group and the control group. This observation was confirmed by measuring the wound areas using specialized software (Image J) (Fig. 7d). Wound areas were estimated using Image J, with wound schematics generated for each group (Fig. 7c), followed by analysis of the wound healing rates (Fig. 7d). As illustrated in Fig. 7d, after `seven days of treatment, the wound area in the HNTs/KGM sponge (H:K=6:10) group was significantly reduced, achieving a healing rate of 72.56 ± 0.03%. The healing rates for the HNTs group, gauze group and blank control group were 78.35 ± 0.03%, 63.93 ± 0.03% and 51.07 ± 5.42%, respectively. By day 14, the HNTs/KGM group and HNTs group attained a healing rate of 96.62 ± 0.01% and 98.64 ± 0.01%, while the KGM group, the gauze group and the control group exhibited a healing rate of 90.55 ± 0.01%, 90.32 ± 0.01% and 86.89 ± 1.37%, respectively, with discernible unhealed lesions still present.

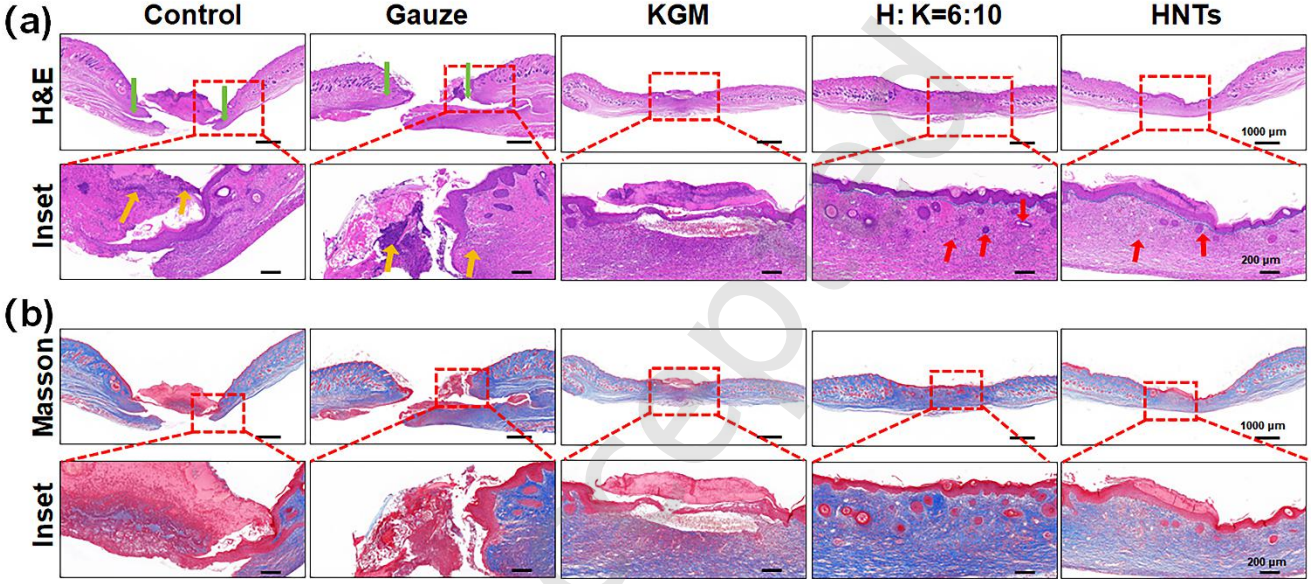


Figure 8 Wound healing performance of different hemostatic materials. Representative images of wound tissue sections in different groups stained by (a) H&E and (b) Masson on day 14 (scale bar = 1000 μm/200 μm).

On day 14, the histopathological structures of regenerated skin in different treatment groups were analyzed using H&E and Masson's trichrome staining. The degree of epidermal regeneration, the extent of inflammatory cell infiltration, and the growth status of skin appendages were used as primary evaluation criteria. The area between the green arrows represents the non-epidermalized region; the blue dashed line indicates the boundary between the epidermis and the dermis; the yellow and red arrows represent inflammatory cells and regenerated skin appendages, respectively. The results of H&E staining (Fig. 8a) revealed that, after 14 days of treatment, the control, gauze and KGM sponge groups still exhibited non-epidermalized areas, discontinuous epidermal regions at the wound sites, and significant infiltration of inflammatory cells surrounding the wounds. Most of the wounds in both control and gauze groups remained unfilled with granulation tissue. Notably, the wounds in the HNTs/KGM sponge group and the HNTs group achieved complete epidermalization, with tight integration at the epidermis-dermis junction. Compared to the control and gauze groups, the HNTs/KGM sponge and HNTs groups exhibited reduced inflammatory cell infiltration, along with a notable neovascularization, hair follicles, and sebaceous glands. Granulation tissue had filled most of the wounds in both the HNTs/KGM sponge group and the HNTs group, collectively indicating superior healing outcomes. This is mainly attributed to the fact that HNTs accelerate wound healing through a multi-path synergistic mechanism. By upregulating the expression of various cytokines and chemokines such as HMMR, S100A14 and CD34, HNTs can promote fibroblast proliferation, migration and extracellular matrix synthesis, as well as induce wound angiogenesis to improve local microcirculation. In addition, HNTs can also markedly boost dermal collagen deposition, facilitate ordered alignment of collagen fibers, and effectively optimize the structural remodeling of the dermis [6, 60, 61].

It is evident that the HNTs/KGM sponge overcame the challenge of difficult HNTs removal while effectively harnessing its potential in promoting wound healing and tissue regeneration, ultimately yielding a more favorable healing outcome compared to the KGM sponge.

Concurrently, Masson's staining further demonstrated that denser collagen deposition and more organized fibrous structures were evident in the granulation tissues of wounds treated with the HNTs/KGM sponge group and the HNTs group (Fig. 8b).

4 Conclusion

In this study, we developed a dual-action, self-gelling HNTs/KGM composite sponge as an outstanding hemostatic agent for irregular bleeding. The material was fabricated via a straightforward freeze-drying process, uniquely integrating the flexibility of a sponge for facile application with the

Under Review

adhesive and retentive properties of an in situ-forming hydrogel.

The hemostatic efficacy of the sponge arises from a robust synergistic mechanism. The highly porous KGM matrix creates a framework for rapid physical absorption of plasma, effectively concentrating red blood cells at the wound site. Simultaneously, the embedded HNTs function as potent biochemical activators, triggering the intrinsic coagulation cascade to promote fibrin network formation.

This composite design exhibited exceptional performance, effectively controlling severe bleeding in a preclinical liver hemorrhage model and tail amputation model, resulting in significantly reduced blood loss compared to commercial gauze. Importantly, the sponge's structural integrity addresses a major translational limitation of powdered hemostats by enabling clean, one-piece removal post-hemostasis, thereby preventing residual particle contamination and minimizing the risk of secondary tissue damage. Additionally, the sponge demonstrates potential to facilitate wound healing. Furthermore, the material exhibits excellent biocompatibility, showing no cytotoxicity and demonstrating superior hemocompatibility.

In summary, the combination of potent dual-action hemostasis, excellent safety profile, and superior handling characteristics positions the HNTs/KGM composite sponge as a highly promising candidate for clinical application in emergency trauma and surgical settings.

Electronic Supplementary Material: Supplementary material (including Optical microscope images, the morphological appearance of sponges and movies) is available in the online version of this article at https://doi.org/ 10.26599/NR.2026.94909248.

Data availability

All data needed to support the conclusions in the paper are presented in the manuscript and the Electronic Supplementary Material. Additional data related to this paper may be requested from the corresponding author upon request.

Acknowledgements

This work was supported by the Guizhou Provincial Science and Technology Projects (Nos. QKHJC-MS[2026]-316, QKHJC-ZK[2021]-161, No. QKHJC-ZK[2021]-263); National Natural Science Foundation of China (No. 52464023); Guizhou Minzu University Scientific Research Fund Project (No. GZMUZK[2022]YB23) ; and Guizhou Provincial Graduate Research Fund Project [No. 2025YJSKYJJ206].

Declaration of competing interest

All the contributing authors report no conflict of interests in this work.

Author contribution statement

Xiaohui Yang: Funding acquisition, Investigation, Methodology, Project administration, Resources, Conceptualization, Writing – review & editing, Supervision.

Haibo Zheng: Data curation, Writing-original draft, Methodology, Investigation, Conceptualization, Formal analysis, Writing – review & editing.

Shaokun Li: Data curation, Investigation, Writing-review & editing.

Yuxin Song: Data curation, Investigation, Writing-review & editing.

Mei Long: Methodology, Conceptualization, funding acquisition, Writing-review & editing, Supervision.

Jun-Long Zhang: Project administration, Funding acquisition, Writing-review & editing, Supervision.

Informed consent

Not applicable.

Ethics statement

The animal experiments were carried out following the guidelines of the Lab of Animal Experimental Ethical Inspection of Dr.Can Biotechnology(Zhejiang) Co., Ltd. and were approved by the Lab of Animal Experimental Ethical Inspection of Dr.Can Biotechnology(Zhejiang) Co., Ltd. (Ethical code: DRK-202504230415).

Use of AI statement

During the preparation of this work, the authors used *Doubao* and *DeepSeek* for language polishing and text refinement, and *Doubao* for the generation of partial schematic elements. All content was fully reviewed, revised, and approved by the authors, who take full responsibility for the scientific accuracy and originality of the manuscript.

References

[1] Lei, X. X.;Liu, M. L.;Lu, C. F.;Han, L. L.;Jia, J. Z.;Li, Z.;Xu, N.;Li, J. F.;Fu, X. J.;Jin, Y. B.;Tong, R. K.;Yu, Y. L.;Luo, G. X.; Chen, Y. A self-hygroscopic, rapidly self-gelling polysaccharide-based sponge with robust wet adhesion for non-compressible hemorrhage control and infected wounds healing. *Bioactive Materials* **2025**, *46*, 311-330.

[2] Yuk, H.;Wu, J.;Sarrafian, T. L.;Mao, X.;Varela, C. E.;Roche, E. T.;Griffiths, L. G.;Nabzdyk, C. S.; Zhao, X. Rapid and coagulation-independent haemostatic sealing by a paste inspired by barnacle glue. *Nature Biomedical Engineering* **2021**, *5*, 1131-1142.

[3] Zhang, K.;Xian, Y.;Li, M.;Pan, Z.;Zhu, Z.;Yang, Y.;Wang, H.;Zhang, L.;Zhang, C.; Wu, D. Gelable and Adhesive Powder for Lethal Non-Compressible Hemorrhage Control. *Advanced Functional Materials* **2023**, *33*, 2305222.

[4] Chen, X.;Yuk, H.;Wu, J.;Nabzdyk, C. S.; Zhao, X. Instant tough bioadhesive with triggerable benign detachment. *Proceedings of the National Academy of Sciences* **2020**, *117*, 15497-15503.

[5] Yu, L.;Shang, X.;Chen, H.;Xiao, L.;Zhu, Y.; Fan, J. A tightly-bonded and flexible mesoporous zeolite-cotton hybrid hemostat. *Nature Communications* **2019**, *10*, 1932.

[6] Feng, Y.;Chen, X.;He, R. R.;Liu, Z.;Lvov, Y. M.; Liu, M. The Horizons of Medical Mineralogy: Structure-Bioactivity Relationship and Biomedical Applications of Halloysite Nanoclay. *ACS Nano* **2024**, 10.1021/acsnano.4c04372.

[7] Guo, B.;Dong, R.;Liang, Y.; Li, M. Haemostatic materials for wound healing applications. *Nature Reviews Chemistry* **2021**, *5*, 773-791.

[8] Zhao, Y.;Abdullayev, E.;Vasiliev, A.; Lvov, Y. Halloysite nanotubule clay for efficient water purification. *Journal of Colloid and Interface Science* **2013**, *406*, 121-129.

[9] Lin, X.;Feng, Y.;He, Y.;Ding, S.; Liu, M. Engineering design of asymmetric halloysite/chitosan/collagen sponge with hydrophobic coating for high-performance hemostasis dressing. *International Journal of Biological Macromolecules* **2023**, *237*, 124148.

Just Accepted

[10] Long, M.;Yang, X.;Shi, T.; Yang, Y. All-natural aerogel of nanoclay/cellulose nanofibers with hierarchical porous structure for rapid hemostasis. *International Journal of Biological Macromolecules* **2024**, *278*, 134592.

[11] Feng, Y.;Luo, X.;Wu, F.;Liu, H.;Liang, E.;He, R.-R.; Liu, M. Systematic studies on blood coagulation mechanisms of halloysite nanotubes-coated PET dressing as superior topical hemostatic agent. *Chemical Engineering Journal* **2022**, *428*, 132049.

[12] Tang, Y.;Wang, N.;Liu, W.;Ding, Q.;Yang, J.;Wu, X.;Cheng, Z.;Hong, B.; Ding, C. The ASB@HNTs-PVA nanofiber membrane, possessing both anti-inflammatory and hemostatic activities, promotes the healing of T2D skin wounds. *International Immunopharmacology* **2024**, *140*, 112780.

[13] Feng, Y.;He, Y.;Lin, X.;Xie, M.;Liu, M.; Lvov, Y. Assembly of Clay Nanotubes on Cotton Fibers Mediated by Biopolymer for Robust and High-Performance Hemostatic Dressing. *Advanced Healthcare Materials* **2022**, 10.1002/adhm.202202265.

[14] Chen, X.;Zhou, Y.;Zhou, S.;Zhang, D.;Zeng, L.;Zhou, C.; Liu, M. 3D printing of chitosan hydrogel reinforced with tubular nanoclay for hemostasis and infected wound healing. *Bioactive Materials* **2025**, *54*, 404-422.

[15] Fan, P.;Zeng, Y.;Zaldivar-Silva, D.;Agüero, L.; Wang, S. Chitosan-Based Hemostatic Hydrogels: The Concept, Mechanism, Application, and Prospects. In *Molecules*, 2023; pp 1473.

[16] Lin, X.;Zhang, D.;Chen, X.; Liu, M. Self-Cross-Linked Oxidized Sodium Alginate/Gelatin/Halloysite Hydrogel as Injectable, Adhesive, Antibacterial Dressing for Hemostasis. *ACS Sustainable Chemistry & Engineering* **2024**, *12*, 11739-11753.

[17] Yoo, J. H.;Yang, D. H.;Choi, J. H.;Nah, H.;Cho, W.;Lee, S. Y.;Lee, J. S.;Kim, H.-J.;Jeong, G.-J.;Chun, H. J.;Heo, D. N.; Kwon, I. K. Sprayable, crosslinker-free, and in situ-forming Schiff-based hydrogels based on oxidized sodium alginate and carbohydrazide-modified gelatin for rapid hemostasis. *Carbohydrate Polymers* **2026**, *373*, 124571.

[18] Rao, K. M.;Prasad, M. S.;Babu, A. G.;Rosaiah, P.;Karim, M. R.; Han, S. S. Tissue adhesive hyaluronan-quercetin (Ago)@halloysite-fungal carboxymethyl chitosan nanocomposite hydrogels for wound dressing applications. *International Journal of Biological Macromolecules* **2025**, *284*, 137849.

[19] Wang, P.;Pu, Y.; He, B. Natural polysaccharide-based hydrogels for hemostasis and wound healing: A review. *Precision Medicine and Engineering* **2025**, *2*, 100016.

[20] Li, Z.;Li, B.;Li, X.;Lin, Z.;Chen, L.;Chen, H.;Jin, Y.;Zhang, T.;Xia, H.;Lu, Y.; Zhang, Y. Ultrafast in-situ forming halloysite nanotube-doped chitosan/oxidized dextran hydrogels for hemostasis and wound repair. *Carbohydrate Polymers* **2021**, *267*, 118155.

[21] Zeng, L.;Chen, X.;Zhou, S.;Zhang, D.;Luo, B.;Zhou, C.; Liu, M. FeS2 nanozymes@halloysite clay nanotube/polyvinyl alcohol/sodium alginate composite hydrogel for hemostasis and bacterial-infected wound healing. *Journal of Colloid and Interface Science* **2026**, *703*, 139120.

[22] Zhao, P.;Feng, Y.;Zhou, Y.;Tan, C.; Liu, M. Gold@Halloysite nanotubes-chitin composite hydrogel with antibacterial and hemostatic activity for wound healing. *Bioactive Materials* **2023**, *20*, 355-367.

[23] Zhou, Z. X.;Li, J.;Hu, J.; Fu, H. Towards promoting wound healing: A near-infrared light-triggered persistently antibacterial, synergistically hemostatic nanoarchitecture-integrated chitosan hydrogel. *Carbohydrate Polymers* **2024**, *329*, 121783.

[24] Zhang, X.;Cheng, F.;Islam, M. R.; Li, H. The fabrication of the chitosan-based bioink for in vitro tissue repair and regeneration: A review. *International Journal of Biological Macromolecules* **2024**, *257*, 128504.

[25] Zhou, X.;Yu, X.;You, T.;Zhao, B.;Dong, L.;Huang, C.;Zhou, X.;Xing, M.;Qian, W.; Luo, G. 3D Printing - Based Hydrogel Dressings for Wound Healing. *Advanced Science* **2024**, *11*.

[26] Wang, Q.;Shi, L.;Li, Y.;Liang, X.;Wang, Z.;Ma, G.;Feng, E.;Yang, Z.; Tian, L. Functional integrated hydrogel with swelling–adhesion, antibacterial and conductive properties for acute wound hemostasis and diagnosis-treatment integration. *RSC Advances* **2026**, *16*, 19674-19686.

[27] Yue, J.;Yao, X.;Li, L.;Liu, W.;Mei, Y.;Midgley, A. C.;Nishinari, K.;Zhao, M.; Li, G. Self-Healing Injectable Double Cross-Linked Hydrogels and Oriented Network-Structured Aerogels as Foodborne Macromolecular Wound Healing Systems. *ACS Applied Materials & Interfaces* **2025**, *17*, 38930-38946.

[28] Chen, H.;Lan, G.;Ran, L.;Xiao, Y.;Yu, K.;Lu, B.;Dai, F.;Wu, D.; Lu, F. A novel wound dressing based on a Konjac glucomannan/silver nanoparticle composite sponge effectively kills bacteria and accelerates wound healing. *Carbohydrate Polymers* **2018**, *183*, 70-80.

[29] Yang, J.; Wang, S. Polysaccharide-Based Multifunctional Hydrogel Bio-Adhesives for Wound Healing: A Review. In *Gels*, 2023; pp 138.

[30] Li, W.;Yang, J.;Kong, W.;Fan, P.;Guan, D.;Bao, Y.;Wu, G.;Wang, S.; Sun, Y. A Polysaccharide - Based Self - Gelling Powder With Antibacterial and Antioxidant Capacities for Acute Hemostasis and Efficient Infected Wound Healing. *Advanced Healthcare Materials* **2025**, 10.1002/adhm.202501101.

[31] Liu, T.;Nong, Z.;Li, Y.;Liu, Z.;Fan, Z.;Liu, H.;Liu, Q.;Qiu, J.;Wang, Q.; Liu, Z. Eutectogel Skin Electrodes with Superior Adhesion, Sweat Resistance, and Long-Term Stability for Electrophysiological Signal Monitoring. *Advanced Functional Materials* **2025**, *n/a*, e03568.

[32] Pan, X.;Zong, Q.;Liu, C.;Wu, H.;Fu, B.;Wang, Y.;Sun, W.; Zhai, Y. Konjac glucomannan exerts regulatory effects on macrophages and its applications in biomedical engineering. *Carbohydrate Polymers* **2024**, *345*, 122571.

[33] Xu, S.;You, J.;Yan, S.;Zhu, L.; Wu, X. Etamsylate loaded oxidized Konjac glucomannan-ε-polylysine injectable hydrogels for rapid hemostasis and wound healing. *Journal of Materials Chemistry B* **2023**, *11*, 9950-9960.

[34] Hao, Y.;Wang, J.;Zhang, H.;Liu, Q.;Wang, X.;Wei, Y.;Liang, Z.;Hu, Y.; Huang, D. Konjac glucomannan/Bletilla striata polysaccharide composite hydrogel: A promising anti-inflammatory dressing for accelerated wound healing. *Carbohydrate Polymers* **2025**, *361*, 123639.

[35] Fan, X.;Li, Y.;Li, N.;Wan, G.;Ali, M. A.; Tang, K. Rapid hemostatic chitosan/cellulose composite sponge by alkali/urea method for massive haemorrhage. *International Journal of Biological Macromolecules* **2020**, *164*, 2769-2778.

[36] Zhang, Y. A. O.;Han, X. A. O.;Zhao, J.;Gan, M.;Chen, Y.;Zhang, J.;He, Y.;Wu, M.; Liu, H. Process optimization and character evaluation of Bletilla striata polysaccharide (BSP) and chitosan (CS) composite hemostatic sponge (BSP-CS). LID - 021002 [pii] LID - 10.1116/6.0003369 [doi].

[37] Teng, L.;Shao, Z.;Bai, Q.;Zhang, X.;He, Y. S.;Lu, J.;Zou, D.;Feng, C.; Dong, C. M. Biomimetic Glycopolypeptide Hydrogels with Tunable Adhesion and Microporous

Under Peer Review

Structure for Fast Hemostasis and Highly Efficient Wound Healing. *Advanced Functional Materials* **2021**, *31*, 2105628.

[38] Wei, X.;Cai, J.;Wang, C.;Yang, K.;Ding, S.;Tian, F.; Lin, S. Quaternized chitosan/cellulose composites as enhanced hemostatic and antibacterial sponges for wound healing. *International Journal of Biological Macromolecules* **2022**, *210*, 271-281.

[39] Mi, Y.;Chen, Y.;Li, Q.;Tan, W.; Guo, Z. pH sensitive adriamycin-incorporated nanoparticles self-assembled from amphiphilic chitosan derivatives with enhanced antioxidant and antitumor activities. *Carbohydrate Polymer Technologies and Applications* **2024**, *7*, 100475.

[40] Naeem, A.;Yu, C.; Wang, X. Highly swellable, cytocompatible and biodegradeable guar gum-based hydrogel system for controlled release of bioactive components of liquorice (Glycyrrhiza glabra L.): Synthesis and evaluation. *International Journal of Biological Macromolecules* **2024**, *273*, 132825.

[41] Zong, S.;Wen, H.;Lv, H.;Li, T.;Tang, R.;Liu, L.;Jiang, J.;Wang, S.; Duan, J. Intelligent hydrogel with both redox and thermo-response based on cellulose nanofiber for controlled drug delivery. *Carbohydrate Polymers* **2022**, *278*, 118943.

[42] Luo, X.;Ao, F.;Huo, Q.;Liu, Y.;Wang, X.;Zhang, H.;Yang, M.;Ma, Y.; Liu, X. Skin-inspired injectable adhesive gelatin/HA biocomposite hydrogel for hemostasis and full-thickness dermal wound healing. *Biomaterials Advances* **2022**, *139*, 212983.

[43] Yang, E.;Hou, W.;Liu, K.;Yang, H.;Wei, W.;Kang, H.; Dai, H. A multifunctional chitosan hydrogel dressing for liver hemostasis and infected wound healing. *Carbohydrate Polymers* **2022**, *291*, 119631.

[44] Zhu, L.;Chen, J.;Mao, X.; Tang, S. A γ-PGA/KGM-based injectable hydrogel as immunoactive and antibacterial wound dressing for skin wound repair. *Biomaterials Advances* **2021**, 10.1016/j.msec.2021.112374.

[45] Madejová, J. FTIR techniques in clay mineral studies. *Vibrational Spectroscopy* **2003**, *31*, 1-10.

[46] Xu, X.;Li, B.;Kennedy, J. F.;Xie, B. J.; Huang, M. Characterization of konjac glucomannan–gellan gum blend films and their suitability for release of nisin incorporated therein. *Carbohydrate Polymers* **2007**, *70*, 192-197.

[47] McDougall, S.;Dallon, J.;Sherratt, J.; Maini, P. Fibroblast migration and collagen deposition during dermal wound healing: mathematical modelling and clinical implications. *Philosophical Transactions of the Royal Society A: Mathematical, Physical and Engineering Sciences* **2006**, *364*, 1385-1405.

[48] Drescher, D.;Büchner, T.;McNaughton, D.; Kneipp, J. SERS reveals the specific interaction of silver and gold nanoparticles with hemoglobin and red blood cell components. *Physical Chemistry Chemical Physics* **2013**, *15*, 5364-5373.

[49] Deng, T.;Gao, D.;Song, X.;Zhou, Z.;Zhou, L.;Tao, M.;Jiang, Z.;Yang, L.;Luo, L.;Zhou, A.;Hu, L.;Qin, H.; Wu, M. A natural biological adhesive from snail mucus for wound repair. *Nature Communications* **2023**, *14*, 396.

[50] Montazerian, H.;Davoodi, E.;Baidya, A.;Baghdasarian, S.;Sarikhani, E.;Meyer, C. E.;Haghniaz, R.;Badv, M.;Annabi, N.;Khademhosseini, A.; Weiss, P. S. Engineered Hemostatic Biomaterials for Sealing Wounds. *Chemical Reviews* **2022**, 10.1021/acs.chemrev.1c01015.

[51] Peng, X.;Xu, X.;Deng, Y.;Xie, X.;Xu, L.;Xu, X.;Yuan, W.;Yang, B.;Yang, X.;Xia, X.;Duan, L.; Bian, L. Ultrafast Self-Gelling and Wet Adhesive Powder for Acute Hemostasis and Wound Healing. *Advanced Functional Materials* **2021**, *31*, 2102583.

[52] Zhao, X.;Huang, Y.;Li, Z.;Chen, J.;Luo, J.;Bai, L.;Huang, H.;Cao, E.;Yin, Z.;Han, Y.; Guo, B. Injectable Self-Expanding/Self-Propelling Hydrogel Adhesive with Procoagulant Activity and Rapid Gelation for Lethal Massive Hemorrhage Management. *Advanced Materials* **2024**, *36*, 2308701.

[53] Malik, U. S.;Niazi, M. B. K.;Jahan, Z.;Zafar, M. I.;Vo, D. V. N.; Sher, F. Nano-structured dynamic Schiff base cues as robust self-healing polymers for biomedical and tissue engineering applications: a review. *Environmental Chemistry Letters* **2022**, *20*, 495-517.

[54] Asadi, L.;Mokhtari, J.; Abbasi, M. An alginate–PHMB–AgNPs based wound dressing polyamide nanocomposite with improved antibacterial and hemostatic properties. *Journal of Materials Science: Materials in Medicine* **2021**, *32*, 7.

[55] Cheng, F.;Liu, C.;Li, H.;Wei, X.;Yan, T.;Wang, Y.;Song, Y.;He, J.; Huang, Y. Carbon nanotube-modified oxidized regenerated cellulose gauzes for hemostatic applications. *Carbohydrate Polymers* **2018**, *183*, 246-253.

[56] Weisel, J. W.; Litvinov, R. I. Red blood cells: the forgotten player in hemostasis and thrombosis. *Journal of Thrombosis and Haemostasis* **2019**, *17*, 271-282.

[57] Colicchia, M.;Schrottmaier, W. C.;Perrella, G.;Reyat, J. S.;Begum, J.;Slater, A.;Price, J.;Clark, J. C.;Zhi, Z.;Simpson, M. J.;Bourne, J. H.;Poulter, N. S.;Khan, A. O.;Nicolson, P. L. R.;Pugh, M.;Harrison, P.;Iqbal, A. J.;Rainger, G. E.;Watson, S. P.;Thomas, M. R.;Mutch, N. J.;Assinger, A.; Rayes, J. S100A8/A9 drives the formation of procoagulant platelets through GPIbα. *Blood* **2022**, *140*, 2626-2643.

[58] Farahani, M.; Shafiee, A. A.-O. Wound Healing: From Passive to Smart Dressings.

[59] Zou, Z.;Zhang, Z.;Ren, H.;Cheng, X.;Chen, X.; He, C. Injectable antibacterial tissue-adhesive hydrogel based on biocompatible o-phthalaldehyde/amine crosslinking for efficient treatment of infected wounds. *Biomaterials* **2023**, *301*, 122251.

[60] Alavi, M.;Totonchi, A.;Okhovat, A.;Motazedian, M.;Rezaei, P.; Atefi, M. The effect of a new impregnated gauze containing bentonite and halloysite minerals on blood coagulation and wound healing. *Blood coagulation & fibrinolysis : an international journal in haemostasis and thrombosis* **2014**, *25*, 856-859.

[61] Xu, R.;Fu, X.;Lun, L.;Jiang, W.;Situ, X.;Huang, X.;Xiong, Y.;Liu, C.; Wang, F. Engineering a halloysite nanotube-enhanced hydrogel 3D skin model for modulated inflammation and accelerated wound healing. *Bioactive Materials* **2025**, *45*, 148-161.

Just Accepted

Electronic Supplementary Material

A self-gelling and easily removable halloysite nanotubes/konjac glucomannan composite sponges for irregular hemorrhage control and wound healing

Xiaohui Yang [1,§], Haibo Zheng [1,§], Shaokun Li [1], Yuxin Song [1], Mei Long [1], and Jun-Long Zhang [2]

[1] *School of Materials Science and Engineering, Guizhou Minzu University, Guiyang 550025, China*
[2] *Beijing National Laboratory for Molecular Sciences, College of Chemistry and Molecular Engineering, Peking University, Beijing 100871, China*
[§] *Xiaohui Yang and Haibo Zheng contributed equally to this work.*

Address correspondence to Xiaohui Yang, xiaohuiyang90@163.com; Mei Long, meilongcsu@163.com; Jun-Long Zhang, zhangjunlong@pku.edu.cn

Supporting information to https://doi.org/10.26599/NR.2026.94909248

Movie S1: Water absorption processes of all sponges.
Movie S2: Bleeding and hemostatic process.

Partial thromboplastin time (PTT)

The PTT test was carried out in accordance with YY/T 1911-2023, the Pharmaceutical Industry Standard of the People's Republic of China: Test Method for Blood Coagulation of Medical Devices [1].

Peripheral blood (20 mL) was collected via vacuum venipuncture from one healthy female volunteer and anticoagulated with 3.2% sodium citrate. Platelet-poor plasma (PPP) was harvested by centrifuging anticoagulated whole blood at 1200 × g for 10 min, and the collected PPP was transferred into a 15 mL centrifuge tube for subsequent experiments. Briefly, 5 mg of each sample was placed in a 1.5 mL centrifuge tube, and 0.4 mL PPP was added to fully submerge the sample. A centrifuge tube containing a 1 × 1 cm glass sheet mixed with 0.4 mL PPP served as the positive control, whereas an empty centrifuge tube supplemented with 0.4 mL PPP was set as the blank control. All samples and controls were incubated at 37 °C with shaking at 60 rpm for 60 min, with three replicates for each group. After incubation, the PPP supernatants were transferred to new tubes, centrifuged at 1000 × g for 10 min, and kept on ice. Prior to measurement, PPP was vortexed for 15 s; 100 µL PPP was pipetted into a coagulation cup and equilibrated at 37 °C for 60 s. Next, 100 µL pre-warmed cephalin suspension was added, mixed, and incubated for 2 min for activation. Subsequently, 100 µL pre-warmed calcium chloride solution (37 °C) was added to initiate the assay, and the PTT was automatically recorded by a semi-automatic coagulation analyzer (SC40, Zhongqin Shidi Biotechnology Co., Ltd., Beijing, China).

Shape recovery ratio

Sample with a diameter of 16 mm was placed on a universal mechanical testing machine (CMT-100N, Huzhou Fanshun Instrument Co., Ltd., China). The sample was compressed at a rate of 2 mm/min. After reaching the preset compressive strain (30%, 50% or 70%), the pressure was maintained for 1 min, and then the load was removed. After 1 min of recovery, the recovered thickness t_1 of the sample was measured. The original thickness of the sample was denoted as t_0. The compression recovery ratio was calculated as:

$$Shape\ recovery\ ratio = \frac{t_1}{t_0} \times 100\% \quad (1)$$

Just Accepted

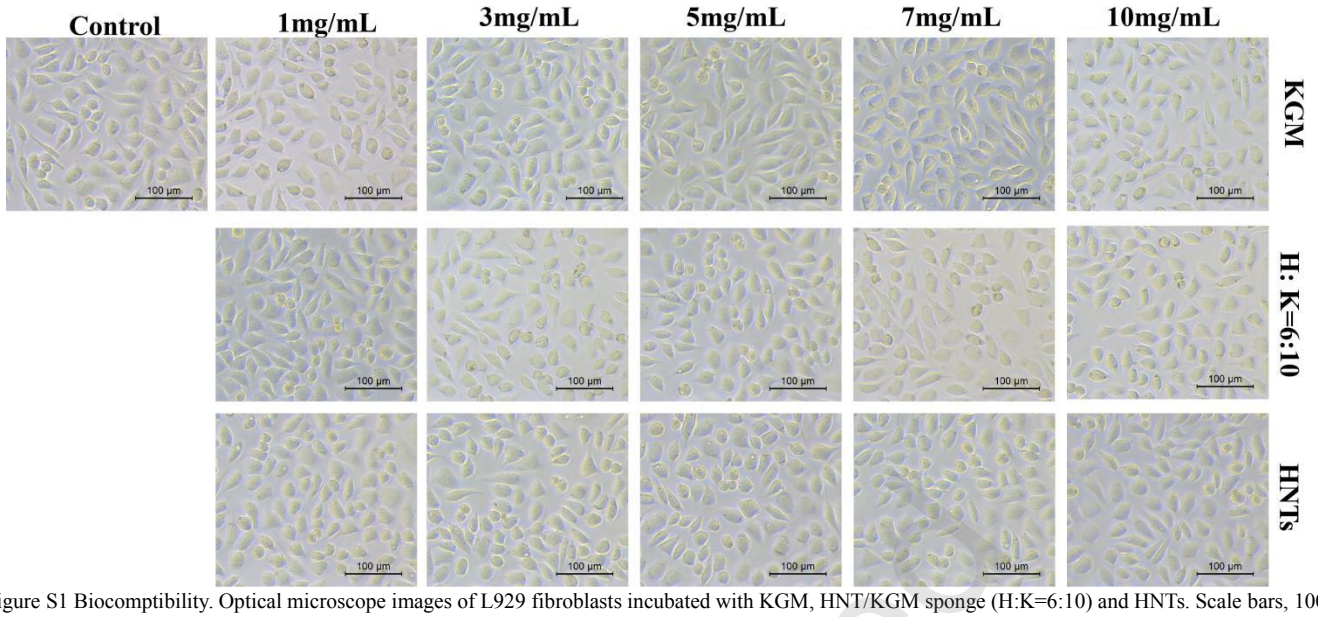


Figure S1 Biocomptibility. Optical microscope images of L929 fibroblasts incubated with KGM, HNT/KGM sponge (H:K=6:10) and HNTs. Scale bars, 100 μm. The cytocompatibility of all materials were evaluated using L929 fibroblasts, a widely recognized cell line for biomaterial testing. Following a 24 h incubation with material extracts, microscopic examination revealed that L929 cells retained a healthy, spindle-like morphology across all test groups, with no discernible differences from the control group.

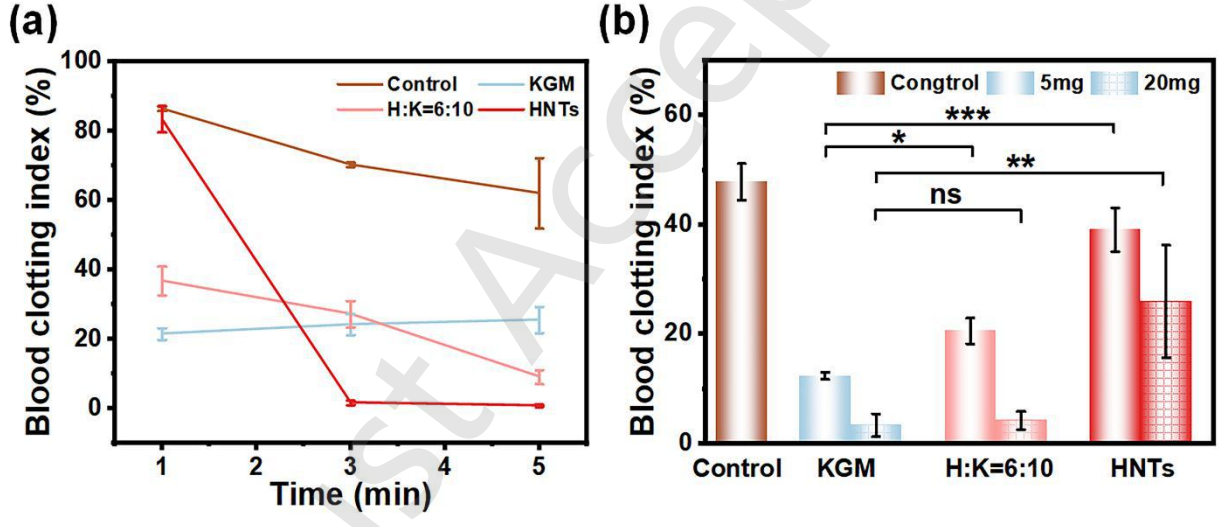


Figure S2 (a). Blood clotting index of HNTs/KGM sponges with varying HNTs ratios and HNTs (1, 3, 5 min). (b). Blood clotting index of KGM and H:K=6:10 sponges with different weights (5 mg and 20 mg, 1min). *p < 0.05, **p < 0.01, ***p < 0.001.

Just Accepted

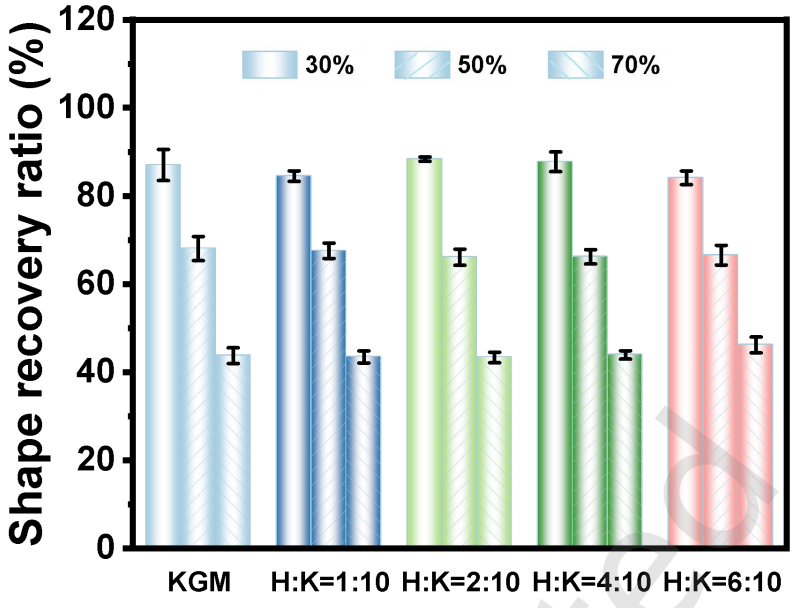


Figure S3 Shape recovery ratio of HNTs/KGM sponges with different HNTs contents after compressive strains of 30%, 50% and 70%. No significant difference in the shape recovery ratio was observed among HNTs/KGM sponges with different HNTs contents ($p > 0.05$).

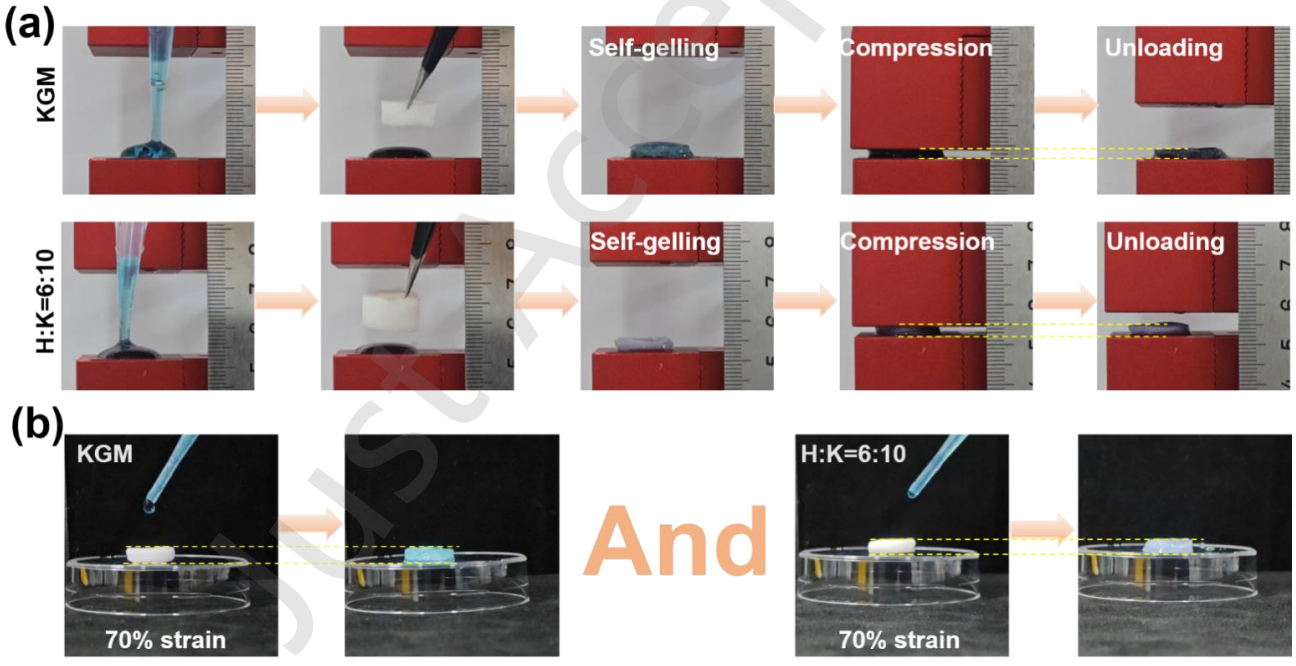


Figure S4 (a) Visual observation on the compression- recovery behavior of self- gelled sponges induced by water. (b) Water- absorbing process of compressed sponges.

Just Accepted

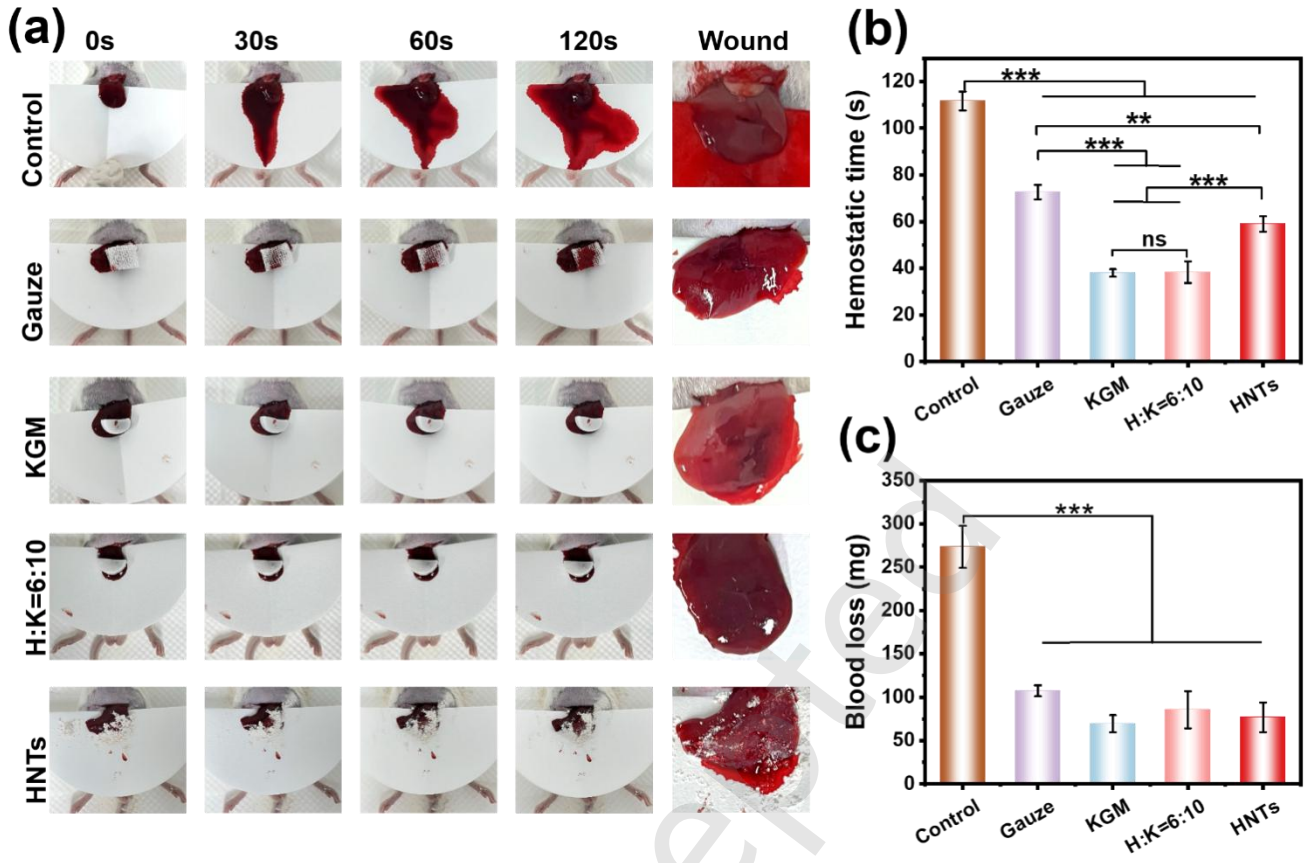


Figure S5 (a) Representative images of hemostatic process. (b)Hemostatic time and (c) relative blood loss of the liver hemorrhage models with milder trauma (wound length: 10 mm; depth: 2 mm) treated with gauze, KGM sponge, HNTs/KGM sponge (H:K=6:10), HNTs. *p < 0.05, **p < 0.01, ***p < 0.001.

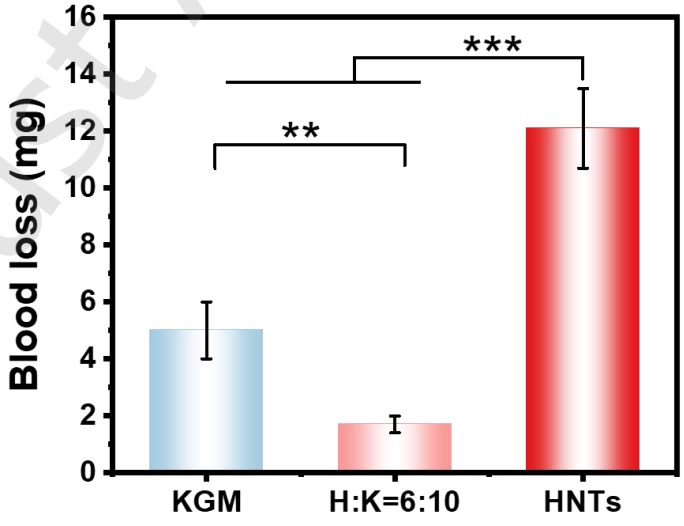


Figure S6 Statistical analysis of blood loss in the mouse tail amputation model for groups treated with KGM sponge, HNTs/KGM sponge (H:K=6:10) and HNTs. *p < 0.05, **p < 0.01, *p < 0.001.

Just Accepted

References

[1] National Medical Products Administration. YY/T 1911-2023, Test method of coagulation for medical devices; 2023.

Just Accepted